

Dipolar interaction between [111] P_b defects at the (111)Si/SiO₂ interface revealed by electron-spin resonance

G. Van Gorp and A. Stesmans

Department of Physics, Katholieke Universiteit Leuven, 3001 Leuven, Belgium

(Received 7 February 1991; revised manuscript received 23 September 1991)

A method is outlined to vary reproducibly the density of [111] P_b centers ($\cdot\text{Si}\equiv\text{Si}_3$ defects with an unpaired sp^3 orbital perpendicular to the interface) at the thermal (111)Si/SiO₂ interface (grown at $\approx 920^\circ\text{C}$; 1.1 atm O₂) using alternate non-*in situ* H passivation (hydrogenation in pure H₂ at temperatures $T=253^\circ\text{C}$ – 353°C) and degassing (high vacuum of $p < 10^{-6}$ Torr at $T=752^\circ\text{C}$ – 835°C). These soft thermal treatments may be randomly sequenced and do not affect the interface structure. Only the spin state (electron spin resonance activity) of P_b centers is modified by bonding or releasing H. The total number of $\cdot\text{Si}\equiv\text{Si}_3$ defects—either passivated or not—remains unaltered and seems to be set by the initial oxidation step. The maximum P_b density is about 1.5% of the Si atom sites in a (111) plane, which appears as a natural constant for the (111)Si/SiO₂ interface thermally grown at $\approx 920^\circ\text{C}$. This [P_b] monitoring is used as a tool to unveil the dipole-dipole (DD) influence on the *K*-band electron-spin-resonance spectrum of P_b centers. The main effects are an overall broadening of the Zeeman resonance and the appearance of fine-structure doublets that grow with increasing concentration. Measurements at low P_b concentrations reveal the residual dangling-bond resonance (void of dipolar interactions). Simulation of this signal using theoretical hyperfine parameters predicted from a relaxed Si₂₂H₂₇ P_b model cluster shows these to be somewhat underestimated. For higher P_b concentrations, dipolar spectra were calculated, starting from a supposed array of possible P_b sites in a (111)Si plane over which the P_b centers are randomly distributed, by exact diagonalization of the spin Hamiltonian for a large number of possible configurations over the array. These are compared with experiments to derive the spatial distribution of the P_b centers. Several site arrays were tested, leading to strong evidence that the P_b centers are randomly distributed over *all* Si atom sites at the interfacial terraces. Models incorporating a strong clustering of P_b centers or correlating them with interfacial steps are excluded. Also, the ditrigonal ring P_b silica-cap model appears inappropriate. Fine structure due to first-, second-, third-, and fourth-neighbor interactions are not observed. This is ascribed to superexchange interaction between neighboring spins; the magnitude of exchange is shown to be compatible with previous observations on other Si dangling-bond-like defects in bulk Si. The superhyperfine structure (of splitting $A_{\parallel}^{\text{shf}} = 14.8 \pm 0.2$ G) due to P_b -electron interactions with ²⁹Si nuclei at second-nearest-neighbor positions in the Si substrate, has conclusively been distinguished from the DD fine structure. Previous investigations of the DD interactions are consistently explained resulting in a consistent picture of the two-dimensional P_b system as regards dipolar and hyperfine interactions, saturation behavior, and moment calculations.

I. INTRODUCTION

Over the past two decades, the interface of thermally grown *c*-Si/SiO₂ structures has received broad attention from both a fundamental- and applied-physics point of view.¹ Various techniques have ascertained it to be atomically abrupt and smooth over macroscopic distances: flat regions of up to ≈ 1000 nm² are separated by ledges typically 1–3 atomic steps high.^{2–4} In spite of this remarkable flatness, it is well documented that the interface houses a significant number of defects.⁵ While most of the interfacial Si atoms are believed to be covalently bonded to interfacial oxygen atoms—thus assuring the tight connection between Si and its high-quality oxide—some interfacial Si orbitals cannot reach a matching O atom. At the (111)Si/SiO₂ interface, electron spin resonance (ESR) has conclusively identified this dominant defect—if not the only one present—as a trivalent interfacial Si atom with an unpaired [111] sp^3 -like hybrid pointing into a microvoid in SiO₂ and backbonded to

three Si atoms in the substrate,^{6–10} it is denoted as $\cdot\text{Si}\equiv\text{Si}_3$, with the dot representing the unpaired electron that makes the defect ESR active. The identification mainly results from the C_{3v} symmetry of the defect, the dangling-bond-like principal values of the *g* dyadic ($g_{\parallel} = 2.0013 \pm 0.0001$ and $g_{\perp} = 2.0086 \pm 0.0003$), and the observation of the ²⁹Si hyperfine lines [both strong hyperfine (hf) and superhyperfine (shf)]. Later on, the model was corroborated by theoretical calculations.^{11–13} Figure 1 shows a schematic of this defect, which is labeled as P_b center when in its neutral ESR-active state.

After conventional (i.e., ≈ 1 atm O₂ ambient; 950°C) thermal oxidation, up to a fraction $f \equiv [P_b]/N_a \approx 0.5\%$ of the $N_a = 7.830 \times 10^{14}$ cm⁻² Si atoms in the (111)Si surface are the site of a P_b center. Combined ESR and electrical measurements^{14–16} have revealed that P_b defects are fast interface states able to trap or lose an electron depending on the Si Fermi-level position. Thus P_b centers emerge as amphoteric centers of positive effective correlation energy $U_e \approx 0.55$ eV. They were shown to account

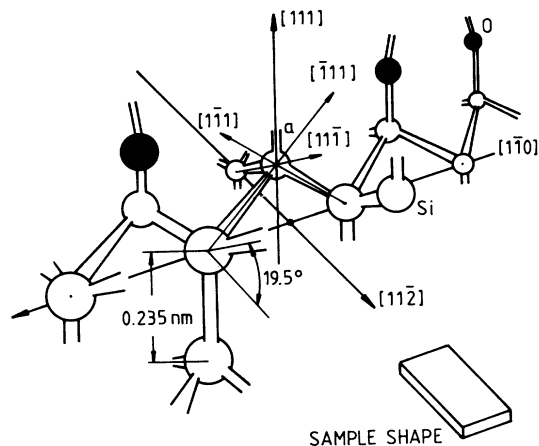


FIG. 1. Schematic view of the atomic configuration at the (111)Si/SiO₂ interface and applied sample geometry. Entity a represents a P_b defect.

for 50–100% of the interface trap density D_{IT} (eV⁻¹ cm⁻²) measured electrically.¹⁵ Hence the unabated interest in their formation kinetics and characterization to atomic detail.

While it has been most intensively studied at the (111)Si/SiO₂ interface, the defect is observed for other interface orientations too,¹ i.e., [100] and [110]. Interestingly, on good-quality (111)Si/SiO₂ it is only the [111] P_b version with unpaired sp^3 hybrid \parallel [111] (perpendicular to the interface) that is observed; those with the unpaired orbital along one of the “equivalent” directions $\bar{[111]}$, $[1\bar{1}1]$, or $[\bar{1}1\bar{1}]$ are not found. The latter only show up in poor-quality¹⁷ structures.¹⁸ Noteworthy is that the occurrence of P_b is not restricted to the Si/SiO₂ interface; it has recently been shown that the $\cdot\text{Si}\equiv\text{Si}_3$ defect is also the dominant defect at the (111)Si/Si₃N₄ interface.¹⁹

The defect's thermochemical interactions^{20,21} are dominated by H. It is believed that bonding to H passivates the center resulting in a neutral diamagnetic defect symbolized as HP_b , which, interestingly, may dissociate again by high-temperature annealing⁷ (pressure $p \leq 10^{-6}$ Torr) at temperatures $T \geq 550^\circ\text{C}$. The large impact this may have on the electrical and technological (e.g., radiation hardness) aspects of the Si/SiO₂ structure has recently stimulated revived interest.

From this short overview, it may appear that P_b has been well characterized. However, various ESR features remain unclear, such as how the P_b centers get rid of excess energy^{20,22} (i.e., spin-lattice relaxation), the linewidth (and line-shape) buildup,^{23,24} and observed K -band ESR intensity anisotropy²³ in (111)Si/SiO₂. Of fundamental interest is the as yet unanswered question about the physical process(es) leading to P_b formation. Likely, key information could come from the knowledge of their distribution: given that they reside essentially in one atomic (interfacial) plane, their areal distribution remains as yet unknown. As inferred from observing only a one-branch ESR spectrum on (111)Si/SiO₂, hardly more is known than that they presumably do not reside preferably near ledges or atomic steps. But are they distributed regularly

or randomly? Or perhaps clustered? Or rather statistically scattered over a less-dense regular pattern of possible sites, as suggested by recent high-resolution transmission electron microscopy (HRTEM) (Ref. 4) and theoretical considerations.¹³ Obviously, all this relates to the ultimate question of how structurally SiO₂ matches to Si. Evidently, as the P_b centers, because of their nature, are intrinsically sensitive *interface probes*, much insight is expected from their full distribution characterization. One possible way—and apparently, so far the only one—leading to that information would be the ESR observation and detailed calculation of the dipole-dipole (DD) interaction among the interface states.

There has been some previous ESR work on this matter. Moment calculations show that the dipolar broadening should be easily observable for a P_b fractional occupancy of 0.5% at the (111)Si/SiO₂ interface.^{25,26} For this, the anisotropy of the peak-to-peak linewidth ΔB_{pp} versus the angle θ between the applied magnetic field \mathbf{B} and the interface was calculated—a typical characteristic of DD interactions in one and two dimensions. However, several scrutinizing measurements^{25,26} failed to resolve any such dependence. Saturation measurements by Braet and Stesmans,²² on the other hand, indicated the P_b resonance line to contain a non-negligible part of homogeneous line broadening—most probably due to dipolar broadening. Finally, an exact calculation by Brower and Headley,²⁴ based on numerically solving the spin Hamiltonian, showed that there should be a small dipolar broadening (of ≈ 0.35 G on the absorption spectrum for $f=0.5\%$ and $\mathbf{B}\parallel[111]$), which should be anisotropic. However, linewidth-versus-magnetic-field measurements failed to resolve this contribution, presumably because of too low a P_b density and lack of controlled variation in $[P_b]$. In spite of the vast computational efforts, the experimental line shape could not be fitted, leaving the effect of dipolar broadening unclear.

The present study divides into two parts. First, it reports on the first observation of DD effects in the ESR signal of P_b defects at the (111)Si/SiO₂ interface. To our knowledge, this even represents the first observation of DD interactions within a two-dimensional (2D) dilute magnetic system. The effects of DD interaction are manifested by variations in linewidth, line shape, and resolved structure of the P_b Zeeman resonance as a function of P_b density. In contrast with previous attempts, these effects could be separated out by studying, at one temperature (4.3 K) and for one magnetic-field orientation ($\mathbf{B}\parallel[111]$), the influence of a systematic and reproducible change in fractional occupancy of (ESR-active) P_b defects. Measuring the influence of systematic variations in spin density on linewidth has turned out to be a far more sensitive means to unveil the DD interaction than analyzing the linewidth anisotropy, previously pursued.²⁴

Second, DD-broadened ESR spectra have been numerically calculated, using a computational algorithm similar to that of Brower and Headley.²⁴ Comparison to the experiment has enabled us to infer information on the in-plane distribution of P_b centers, which relates to their role in the Si/SiO₂ interface growth. The experiments also provide useful information on the residual line shape,

that is, the shape in absence of dipolar broadening, to which the calculations of Cook and White¹³ are compared.

The overall objective of this work is to provide information on the nature of the DD interaction between P_b centers at the (111)Si/SiO₂ interface, and to infer the spatial distribution, which is of fundamental interest. Much of the success in detection of the DD effects in ESR spectra depends on the reproducibility of (hydrogen) passivation of P_b defects, that is, reversibly switching them between the neutral, ESR-active paramagnetic state ($\cdot\text{Si} \equiv \text{Si}_3$) and a diamagnetic complex, e.g., HP_b . This thermal passivation-depassivation procedure, based on alternated hydrogenation and vacuum treatments, has been systematically analyzed using the ESR properties of P_b centers as a diagnostic tool. This procedure is then used as a tool to disclose the DD effects within the 2D P_b system.

II. EXPERIMENTAL PROCEDURES

A. Sample preparation

Starting material consisted of 3-in Czochralski-grown B-doped (111)Si wafers of room-temperature (RT) resistivity $\rho = 10 \pm 2 \text{ } \Omega \text{ cm}$, thinned down to a thickness $d_{\text{Si}} = 117 \pm 16 \text{ } \mu\text{m}$ and polished to optical flatness on both sides. Using a diamond saw, the wafers were cut into slices of $1 \times 9 \text{ mm}^2$ main surface, which had their long edge along the $[11\bar{2}]$ crystal axis (see Fig. 1). Typically, 10–15 slices were stacked to enhance the effective interface area ($\approx 2\text{--}3 \text{ cm}^2$) in the cavity.

Prior to oxidation the platelets were thoroughly cleaned using a standard procedure described elsewhere.²⁷ The last rinse before transferring the slices to the oxidation setup was in acetone. All chemicals used were of metal-oxide-semiconductor (MOS) (low sodium content) quality.

Thermal treatments were carried out in a conventional setup consisting of a double-wall fused-silica that could be offset from the resistance-heated furnace. The processing gas composition was continuously monitored by means of a quadrupole mass spectrometer (type VG Argon). This laboratory preparation system has exclusively been used for thermal treatment of high-purity Si and was regularly checked to be He leak tight to better than $10^{-10} \text{ Torr l/s}$.

Three ESR samples (S1, S2, and S3) were studied, which were submitted to essentially three types of thermal treatments, that is, oxidation, hydrogenation, and vacuum degassing, alternated with diagnostic ESR measurements. S1 and S2 were oxidized in dry oxygen (99.999% pure) at a pressure p_{O_2} of about 0.2 atm for a time t_{O_2} of, respectively, 63 and 84 min at a temperature $T_{\text{ox}} = (920 \pm 15)^\circ\text{C}$; this resulted in oxide layers of thickness $d_{\text{SiO}_2} = 134$ and $152 \pm 5 \text{ } \text{Å}$, respectively. Appropriate use of liquid-nitrogen baffles assured a dry thermal oxidation. Oxidation of sample S3 in dry flowing oxygen at $p_{\text{O}_2} \approx 1.1 \text{ atm}$ during 130 min at $(956 \pm 15)^\circ\text{C}$ resulted in oxide layers of $d_{\text{SiO}_2} = 637 \pm 13 \text{ } \text{Å}$. Oxidation was initiated

by rolling the furnace to the fused-silica tube filled with 99.9999%-pure N₂ gas and switching the N₂ gas to pure O₂ after a few pump cycles. It was quenched by either evacuating the silica tube or changing the ambient to N₂ again and rolling away the furnace. The samples were allowed to cool to room temperature. They remained in the sample tube till a first ESR measurement on the oxidized state to characterize the P_b defects.

Subsequently, two types of heat treatment were repeatedly alternated to vary the concentration of the spin-active interface defects. These were either hydrogenation in order to passivate (part of) the P_b system by bonding to H or a (partial) dehydrogenation in vacuum to raise the spin concentration. Hydrogenation treatments were carried out in a 99.9999%-pure H₂ flow at $p_{\text{H}_2} \approx 1.1 \text{ atm}$ for times t_{H_2} and temperatures T_{H_2} in the range of 11–79 min and 253°C – 353°C , respectively. The process was stopped by removing the hydrogen and offsetting the furnace. Depassivation treatments, instead, were performed in vacuum ($p \leq 2.0 \times 10^{-7} \text{ Torr}$) pumped by a turbomolecular pump for times t_D and temperatures T_D in the range $110 \leq t_D \leq 150 \text{ min}$ and $752 \leq T_D \leq 835^\circ\text{C}$. The samples were thoroughly cleaned in acetone prior to each passivation or depassivation treatment. They were kept at RT in air between measurements. Unlike previous passivation experiments,²⁰ a set of hydrogenation and dehydrogenation cycles were carried out on *one* sample. This allowed us to analyze the reversibility of the passivation-depassivation process, that is, to check for any eventual irreversible structural rearrangements of the interface reflected by variations in the ESR characteristics of the P_b centers.

B. ESR spectrometry

Most ESR measurements were carried out at about 4.2 K using a *K*-band ($\approx 20.2 \text{ GHz}$) homodyne reflection spectrometer of the balanced-mixer type driven in the absorption mode under adiabatic slow passage. Some controlling observations were carried out in an *X*-band (9 GHz) setup (4–15 K; incident microwave power $P_\mu \leq 1 \text{ } \mu\text{W}$) exhibiting a much lower sensitivity, however. Sinusoidal modulation at 100–150 kHz of **B** allowed phase-sensitive detection resulting in the detection of absorption-derivative spectra $dP_{\mu a}/dB$; $P_{\mu a}$ represents the absorbed microwave power in the high-purity copper TE₀₁₁ cylindrical cavity.

As the aimed experimental observations and accuracies required an utmost spectrometer sensitivity at low P_μ , some special precautions were taken. A top-loading system was designed that enabled insertion of the sample in the cavity while the cryostat remained at 4.3 K. This allowed a correct positioning of the sample stack inside the cavity. Together with the remotely tuned cavity coupling, this permitted the tuning of the system for the maximum loaded-cavity quality factor ($Q_L \approx 13\,000\text{--}16\,000$). When optimized, the spectrometer could detect about 4×10^{10} P_b defects/*G* linewidth in a single magnetic-field trace at 4.3 K with a signal-to-noise (*S/N*) ratio of ≈ 1 using $P_\mu = 2 \text{ nW}$, a lock-in time con-

stant $\tau=1$ s, and an optimum modulation field amplitude B_m . The noise figure of the 1N26 detection diodes was 9.0 dB. Together with signal averaging facilities (typically 10–30 traces) and the application of low B_m (typically $\leq 0.2\Delta B_{pp}$) this permitted us to measure accurately low-concentration P_b resonances and linewidths without any overmodulation or saturation effects. No digital filtering was used throughout. The strong saturability of P_b centers at 4.3 K necessitated the use of very low microwave power to avoid saturation effects—power levels as low as $P_\mu = -63$ dBm (0.5 nW) were used, which did not prevent measurements at 4.3 K in the K band. Obvious advantages of the liquid-He temperature measurements are the enhanced susceptibility χ (for P_b , $\chi \sim 1/T$) and the higher cavity Q_L —as we use Si samples with $\rho \approx 10$ Ω cm, generation of free carriers results in a vanishing Q_L above 35 K, thus preventing ESR observations. Measurements were routinely carried out for $\mathbf{B}||[111]$ as to obtain the most favorable S/N ratio. It is known that,^{23,28} as \mathbf{B} is tilted away from [111], the P_b signal broadens due to strain broadening of g_\perp with attendant reduction in S/N ratio.

In contrast with a previous conclusion,²⁰ we obtain the best S/N ratio at the lowest temperatures. The strong saturability, though, of the P_b signal at 4.3 K would suggest measurements at higher T to be more favorable: with increasing T , the P_b resonance will become less sensitive to level population distortions (saturation) as the spin-lattice relaxation time T_1 decreases.²² This, however, results in a degraded S/N ratio for the present setup for various reasons. First, there is the obvious decrease in signal intensity due to variation in Boltzmann factor describing the difference in Zeeman level population. Second, the present samples concern commercial Si doped to $[\mathbf{B}] = (1.3 \pm 0.3) \times 10^{14}$ cm^{-3} of typically $\rho_{RT} \approx 10$ Ω cm, that is, no intrinsic high-purity Si of $\rho \geq 1000$ Ω cm. This causes a steady decrease in Q_L due to enhanced microwave dissipation in the Si substrate by the growing extrinsic carrier concentration as T increases. Third, spectrometer instabilities due to, e.g., microphonics, become more critical at higher T . These instabilities are relatively more detrimental the smaller the signal to be measured.

Measurement of the (spin) density $[P_b]$ (cm^{-2}) of P_b defects of spin $S = \frac{1}{2}$ has received special care. Not only is it a main quantity in the DD interaction, but also, the absolute determination of the number of spins in a sample to a satisfying accuracy is very difficult in general. The reason is the numerous spectroscopical and geometrical factors—some of which are difficult to control—that may have an influence. If not properly addressed, the quoted values rarely reach a 50% confidence level. Numbers of spins were determined relative to a spin concentration standard by comparing the intensity I (area under the absorption curve) of both signals, as obtained by double numerical integration of the respective $dP_{\mu a}/dB$ spectra recorded in *one* trace. Both signals have conscientiously been checked for each measurement for any spectroscopical distortions such as overmodulation, saturation, or dispersion admixing.

The spin standard, basically, is a ruby ($\text{Al}_2\text{O}_3:\text{Cr}^{3+}$) platelet (obtained from the National Bureau of Standards) of which the number of spins at RT is specified to an accuracy of $\pm 1\%$. Yet, for practical and sensitivity reasons, it is not this sample which has been attached to the unknown sample in the cavity. Instead, a secondary standard²⁹ consisting of *c*-Si:P powder of $[\text{P}] = 1.7 \times 10^{18}$ cm^{-3} —calibrated at 4.3 K against the ruby—is used for practical and sensitivity reasons. The accuracy reached will depend on various factors, such as, integration errors, spectroscopical (e.g., the microwave field intensity sensed by both samples), geometrical (e.g., sample size and positioning in the cavity), and the reference sample accuracy. There are two items of concern regarding the spin standard, namely, the calibration *accuracy* and *temperature*. First, the standard's number of spins needs to be known at the temperature of $[P_b]$ measurement, that is, 4.3 K. The RT spin density can only be transferred to the signal intensity at low T if having theoretical understanding of the χ -versus- T behavior. The χ -versus- T relationship of the ruby sample has been checked in detail against a metallic LiF:Li marker.^{30,31} A Curie-law ($\chi \propto T^{-1}$) behavior has been found down to 4.3 K, as expected for a diluted concentration of magnetic impurities in an insulating matrix. The same remark applies to the “unknown” P_b signal, which also exhibits a $\chi \propto T^{-1}$ dependence.

Second, regardless of the fact that its number of spins has been quoted very accurately, the ruby has been extensively cross checked at 77 K against two independent markers; first, a powder of *c*-Si:P doped to the submetallic concentration²⁹ of $[\text{P}] = 1.7 \times 10^{18}$ cm^{-3} , and, second, to low-concentration P-doped Si ($[\text{P}] \approx 10^{14}$ cm^{-3}), of which the number of spins was independently determined from the sample's conductivity and weight. Agreement is found within 20% in both cases. Hence, it is concluded that the accuracy reached on $[P_b]$ is determined by geometrical factors and integration accuracies, the latter likely being predominant for the broad-winged P_b signals. The absolute accuracy typically obtained is estimated at $\pm 10\%$, while a relative accuracy of $\pm 5\%$ may have been reached when comparing the P_b density of one sample over various thermal treatments.

III. EXPERIMENTAL RESULTS AND DISCUSSION

The width ΔB_{pp} of the P_b resonance, observed at $g = 2.0014$, for $\mathbf{B}||[111]$, is plotted versus spin concentration (and fractional site occupancy) for three samples ($S1$, $S2$, and $S3$) in Fig. 2. Concentrations are obtained by comparison of the areas under the absorption curves of the P_b and spin marker signals, as outlined before. As the areas are calculated by double numerical integration over a magnetic-field window of typically 25–50 G about the center of resonance, the unpaired electrons at ²⁹Si P_b nuclei (nuclear spin $I = \frac{1}{2}$; 4.70% natural abundance), which show a strong hf splitting (≈ 156 G), are not taken into account; this will have to be corrected for when comparing to theory. Figure 2 also shows the $[P_b]$ dependence of two other ESR properties, i.e., the absorption

linewidth at half height ΔB and the line-shape factor κ , defined as $\kappa = I / (V_D \Delta B_{pp}^2)$, where $2V_D$ represents the peak-to-peak height of the $dP_{\mu a} / dB$ curve. Data were obtained, as outlined, by varying the P_b concentration of a sample by alternate post-oxidation hydrogenation and dehydrogenation treatments. This is most clearly illustrated in Fig. 2 for sample S1, for which the ΔB_{pp} data points are labeled by letters ($a-n$) in order of their processing and measuring sequence. This brings out the influence of the step-by-step processing. Point a is mea-

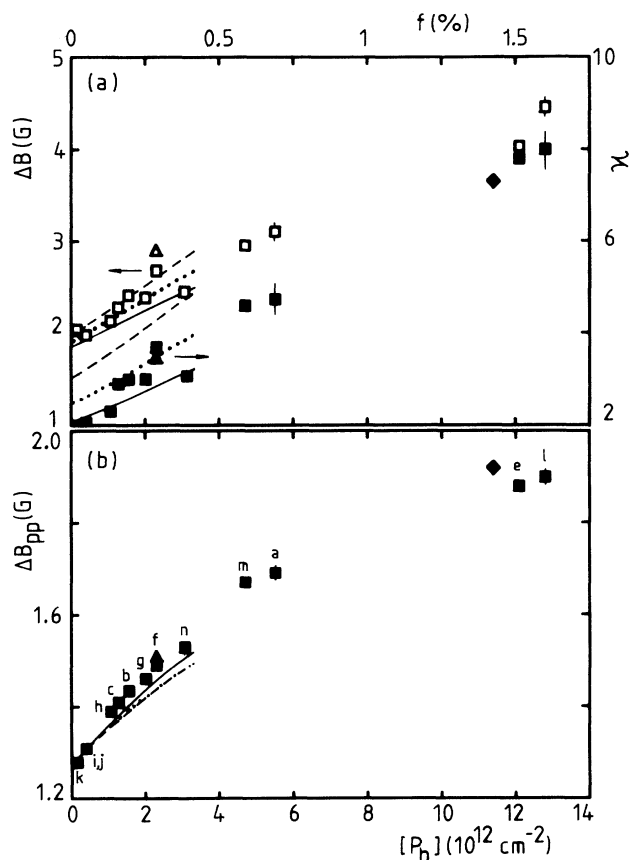


FIG. 2. Plot of the K -band (4.3 K) absorption linewidth ΔB [open symbols in (a)], the line-shape factor κ [closed symbols in (a)], and the absorption derivative linewidth ΔB_{pp} (b) of the $[111] P_b$ defect at the $(111)\text{Si}/\text{SiO}_2$ interface vs P_b density for three samples: S1 (■), S2 (▲), and S3 (◆). The S1 data were obtained on one sample by sequential hydrogenation and dehydrogenation treatments, of which the sequence is denoted by the alphabetical labeling of the data. The last thermal treatment the sample received prior to each ESR measurement is discussed in the text. The curves are theoretical fits obtained by numerical calculation of the dipolar histogram vs $[P_b]$, assuming that all Si atoms in an unreconstructed $(111)\text{Si}$ interface plane may be the site of a P_b defect (the most general array of possible sites model), over which the defects are randomly distributed. Convolution of the dipolar histograms with three types of residual line shapes leads to the dashed, dotted, and solid curves for the residual shapes $R1$, $R2$, and $R3$, respectively. These residual shapes are estimates for the $[P_b] \rightarrow 0$ shape (i.e., void of dipolar interaction effects) as explained in the text. The spin concentrations are obtained by double numerical integration over a 25–50-G sweep, relative to a spin standard.

sured on the as-oxidized state (0.2 atm O_2 at 920°C), characterized by a fractional P_b site occupancy of $f \approx 6 \times 10^{-3}$ —a typical value for dry oxidations. Subsequently, three passivating steps were performed on S1: hydrogenation at 253°C for 37 min (b), at 253°C for 43 min (c), and at 353°C for 19 min (d), respectively. Point d , however, is not shown in Fig. 2, as in this case the interface defects were passivated below the detection limit. The next to the highest spin density and linewidth (point e) was found by a degassing treatment at $(743 \pm 15)^\circ\text{C}$ for $t_D = 138$ min, resulting in $[P_b] = (12.1 \pm 0.6) \times 10^{12} \text{ cm}^{-2}$ and $\Delta B_{pp} = 1.88 \pm 0.02$ G. This was followed again by hydrogenation treatments (points $f-k$ in Fig. 2), and a new dehydrogenation step (l ; 150 min at 835°C), resulting in about the same “maximum,” i.e., $[P_b] = (12.8 \pm 0.8) \times 10^{12} \text{ cm}^{-2}$ and $\Delta B_{pp} = 1.90 \pm 0.2$ G. Finally, this was followed again by passivation treatments (points m and n in Fig. 2) for 10–33 min at 279°C . The triangle and diamond symbols in Fig. 2 are data obtained on samples S2 and S3 (dehydrogenated at 827°C for 123 min), respectively.

The increase of linewidth with increasing P_b concentration is strong evidence for DD interactions between the interface spins. Indeed, as f increases, the interdefect site distance decreases, resulting in an increase of the dipolar broadening. Other line-broadening mechanisms involved, such as unresolved hyperfine broadening,²³ do not show such dependence on f . In another interpretation, however, one could attribute the observed ΔB_{pp} - f behavior to variations in strain broadening²³ resulting from interfacial strain adjustments attending the various thermal steps. Strain broadening is a g -tensor broadening resulting from local variations in interface strain that produce a site-dependent modulation of the defect’s structure. This alternative, however, is untenable. First, it disagrees with the reproducibility of the ΔB_{pp} - f data: the results convincingly show that one can move reproducibly up and down the ΔB_{pp} -versus- f curve by sequential H-related defect passivation and depassivation thermal steps. These steps, apparently, may be arbitrarily alternated and sequenced; the resulting data points all assemble around a common curve. This is true for all three samples, oxidized under different circumstances. This clearly suggests that there exists a universal ΔB_{pp} - f relationship, at least for the $(111)\text{Si}/\text{SiO}_2$ interface and K -band observational frequency. This behavior, obviously, is in conflict with eventual changes in strain broadening resulting from thermally induced variations in the physicochemical structure of the Si/SiO_2 interface, e.g., stress relaxation. Such thermal relaxation effects would exhibit an irreversible character, leading to hysteresis effects on the linewidth data, unlike experimental observation. Second, for high-quality thermally grown oxides, no influence of strain broadening on the linewidth for $B \parallel [111]$ is expected to first order, anyway.²³

The existence of a universal ΔB_{pp} - f relation, in fact, is as expected along this interpretation: As long as the P_b linewidth (line shape) is determined exclusively by unresolved hyperfine and dipolar broadening and not by strain broadening, this curve has to be universal, also for other Si interface orientations. A promising conclusion

then is that this ΔB_{pp} -versus- f relationship may be used reversibly, that is, accurate measurement of ΔB_{pp} , at whatever microwave frequency, will unequivocally provide the sample's P_b concentration, provided, of course, that the correct spectroscopy is applied to record undistorted signals.

The maximum $[P_b]$ measured seems typical for the (111)Si/SiO₂ interface grown at $T \approx 920^\circ\text{C} - 960^\circ\text{C}$. Whatever dehydrogenation conditions, no P_b fractional occupancy higher than $f_{\max} \approx 0.015$ ($[P_b]_{\max} \approx 1.2 \times 10^{13} \text{ cm}^{-2}$) can be obtained on samples S1 and S3. This evokes the question of whether f_{\max} , indeed, represents the density of all $\cdot\text{Si} \equiv \text{Si}_3$ defects $[P_b]^*$ (including both the paramagnetic, ESR-active P_b centers and passivated $\cdot\text{Si} \equiv \text{Si}_3$ defects) typically left at the (111)Si/SiO₂ interface after thermal oxidation at $\approx 920^\circ\text{C}$. Put otherwise, are all $[P_b]^*$ defects activated by the dehydrogenation treatment? The variations in degassing (vacuum) temperature and time and oxidation circumstances strongly suggest it is. Consequently, this would indicate that $[P_b]_{\max} = [P_b]^*$, the total number³² of trivalent Si defect sites at the (111)Si/SiO₂ interface grown at $\approx 920^\circ\text{C}$. This has been confirmed by extending experiments to various Si/SiO₂ structures, grown under broadly varying circumstances.³³ It thus appears that, for a (111)Si surface, $[P_b]^*$ is primarily set by T_{ox} and the nature of the grown-on insulator.

The data suggest that H—intentionally or not—has been the ubiquitous passivating agent of interface defects in Si/SiO₂ growth. This is corroborated by the data in the literature exhibiting a broad variation in electrically active (unpassivated) fast interface state trap density over various preparation setups.³⁴ An unintentional passivation effect may also be seen in Fig. 2. Although we took firm measures to grow the oxides as dry as possible, a partial incorporation of H at the interface seems unavoidable, as shown by comparison of the maximum (cf. points *e* and *l* in Fig. 2) and as-oxidized (cf. point *a* in Fig. 2) P_b concentrations.³⁵ Hydrogen, almost unavoidably, abounds, i.e., as an impurity in the native oxide and oxidizing ambient, where it will further be enhanced by permeation through the walls of fused-silica tubes surrounding the samples during oxidation.

As shown in Fig. 2, the linewidth variations versus f are accompanied with unusually large variations of κ , increasing from $\kappa \approx 2$ for $f \rightarrow 0$ to $\kappa \approx 7.9$ for f_{\max} . It is clearly seen that the description of the line shape by a Voigt profile (convolution of a Lorentzian and Gaussian), as is practiced for low-density P_b signals,^{23,36} fails for the highest P_b concentrations: The Voigt profile of highest κ is a Lorentz curve with $\kappa = 3.63$. It follows that the line shape of the dominant broadening mechanism for high $[P_b]$ has to be characterized by $\kappa \gtrsim 8$. Such a high κ is unrealistic for a strain-broadening mechanism of any kind (usually a Gaussian profile). It is, however, quite feasible for the dipolar spectrum of a dilute 2D spin system, as will be shown in the next section, and points to a (partially resolved) multiline spectrum.

Extrapolation of the ΔB_{pp} -versus- f relationship towards $f \rightarrow 0$ leads to the *residual* natural width (that is,

natural width void of DD broadening) $\Delta B_{pp}^R = 1.29 \pm 0.03$ G. The corresponding signal has a line-shape factor $\kappa = 2.0 \pm 0.1$. For the integrated spectrum, we obtain the width $\Delta B^R = 1.98 \pm 0.03$ G, giving $\Delta B^R / \Delta B_{pp}^R = 1.53 \pm 0.06$. This is to be compared with the Voigt-function value $\Delta B / \Delta B_{pp} (\kappa = 2.0 \pm 0.1) = 1.40 \pm 0.02$, indicating that the residual P_b signal, like the high- f signals, has no perfect Voigt shape. If, nevertheless, interpreting the residual signal along a Voigt shape, it follows that the best fit is obtained with $\Delta B_{pp}^{L,R} = 0.67$ G and $\Delta B_{pp}^G = 0.90$ G for the peak-to-peak width of the constituent Lorentzian and Gaussian broadening function, respectively. A previous²³ self-consistent analysis on a somewhat-higher- f sample (quoted as $3 \leq [P_b] \leq 5 \times 10^{12} \text{ cm}^{-2}$) also concludes a Voigt shape, but with $\Delta B_{pp}^L = 1.14$ G and $\Delta B_{pp}^G = 0.49$ G—clearly bearing out the higher f . As the exact knowledge of the residual line shape is of primary importance to predict the correct line shape in the case of DD interactions, a detailed theoretical study of the residual line will be carried out in the next section.

Figure 3 shows P_b signals for different values of f measured on sample S1 for $\mathbf{B} \parallel [111]$. Clearly, there is a distinct evolution from a narrow, featureless (at least, within measurement accuracy) signal for $f \rightarrow 0$ (labeled *A*) to an intense, multistructured signal at $f \approx 0.015$. As the resolved structures are doublets (labeled as *B*, *C*, and *D* in Fig. 3) centered at the central signal *A*, they can originate either from hyperfine or DD interactions. It is known, however, that the hf interaction with ²⁹Si nuclei does not depend on $[P_b]$, so that the relative hf signal intensity should not vary with increasing f . Moreover, as the ²⁹Si natural abundance is $\approx 4.70\%$, no intense hf structure is expected. Hence, doublet *B* can be quite certainly identified as fine structure due to DD interactions, not hyperfine, since at f_{\max} the intensity of doublet *B* surmounts the intensity of the central line. The assignment of the overlapping doublets *C* and *D* is more subtle—doublet *D* outgrows doublet *C* only at higher f —and must await the theoretical analysis of the DD-broadened spectra, as explained below. Yet, doublet *C*, whose relative intensity appears little affected by variations in f , may be ascribed to ²⁹Si hf interactions. There is theoretical evidence^{11–13} for the existence of such a hf doublet with a splitting of 13.0 ± 4.0 G. It is ascribed to a (weak) interaction of the unpaired P_b electron with ²⁹Si nuclear spins at the three second-nearest-neighbor sites in the substrate, and has been interpreted along these lines.^{10–13} This assignment is corroborated by the present systematic analysis of DD-induced fine structure, leading to unequivocal identification of the various doublets.

The other structure with larger splittings has patiently been looked for at 4.3 K using different magnetic-field windows, covering the whole field range between the central line *A* and the strong ²⁹Si hyperfine doublet; this hf doublet originates from interaction of the unpaired P_b electron with the nuclear spin ($I = \frac{1}{2}$) of the central ²⁹Si atom.⁹ This search, however, was unsuccessful, even after continued signal averaging, of up to ≈ 100 field scans. It is the fine structure, or else the lack of struc-

ture, that is particularly analyzed in the light of the present understanding of DD interactions to acquire information on the in-plane distribution of P_b centers.

IV. THEORY: CALCULATION OF THE DD-BROADENED ESR SPECTRUM OF A DILUTE 2D SPIN SYSTEM

In this section we present a theoretical justification for the interpretation of the experimental data, outlined in Sec. III, assuming the residual line ($f \rightarrow 0$) to be dominated by unresolved hyperfine broadening and the f -dependent broadening to be of dipolar origin. This justification comprises mainly a quantitative prediction of the f dependence of measured quantities as shown in Figs. 2 and 3 and, at the same time, a detailed approximation of the experimentally obtained line shapes for all f .

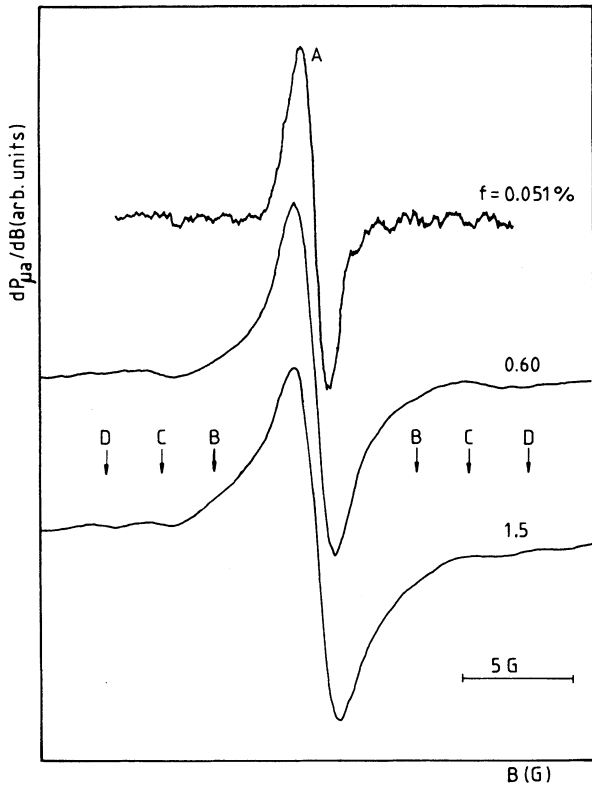


FIG. 3. K-band (≈ 20.2 GHz) absorption-derivative ESR spectra of $[111]$ P_b defects (unpaired sp^3 orbital perpendicular to the interface) located at the $(111)\text{Si}/\text{SiO}_2$ interface observed at 4.3 K with $P_\mu \leq -63$ dBm and $\mathbf{B} \parallel [111]$ for various P_b fractional occupancies f . The central Zeeman signal A of $g = 2.00138 \pm 0.00005$ is seen to broaden with increasing $[P_b]$, while it develops distinct shoulders (doublet B) ascribed to fine-structure resulting from dipolar interaction. This doublet grows in intensity relative to the central signal A . The region around doublet C , which is ascribed to superhyperfine structure, clearly develops more structure at higher f . The well-resolved doublet D is ascribed to fine structure (fifth-neighbor pair interaction).

A. Previous calculations and evidence for DD interaction

The previous calculations divide into two main parts: (1) the method of moments, and (2) the computational-statistical approach. In this section, we will deal only with the method of moments; the computational approach will be dealt with in detail in Sec. IV C, as it is also the underlying approach used in our calculations. In addition to the method of moments, we will discuss some early experimental evidence for the DD interaction between P_b defects, as obtained by ESR saturation theory.³⁷

1. Moment calculations

Although it was impossible to obtain an analytical expression of the resonance line shape, broadened by dipolar and exchange interactions, for a great number of spins in a (3D) crystal, Van Vleck³⁸ found that the *moments* of the resonance line could be worked out analytically. He also showed that, in principle, when all moments are known, the line shape can be derived from them. In practice, calculations never go beyond the fourth moment, so that only a very limited knowledge is obtained of the line shape (linewidth). If, however, the line shape is well characterized, the second moment (M_2) permits the calculation of the linewidth quite accurately for a three-dimensional spin system. The fourth moment (M_4) may be used as a check for the line shape. In the case where the magnetic spins are randomly distributed over the crystal with a fractional occupancy f and the exchange interactions may be neglected, the Van Vleck expressions for the second and fourth moments, as rewritten by Kittel and Abrahams³⁹ and Canters and Johnson,⁴⁰ are given as

$$M_2 = f \frac{S(S+1)}{3h^2} \sum_{\substack{k \\ (k \neq j)}} B_{jk}^2, \quad (1)$$

$$M_4 = f \frac{S(S+1)}{3h^2} \left[\frac{f}{3} \sum_{\substack{k,l \\ (j \neq k \neq l \neq j)}} [B_{jk} B_{jl} (7B_{jk} B_{jl} + 2B_{kl}^2)] \right. \\ \left. + \frac{1}{5} \left[7 - \frac{3}{2S(S+1)} \right] \sum_{\substack{k \\ k \neq j}} B_{jk}^4 \right], \quad (2)$$

with

$$B_{jk} = \frac{3\mu_0 g^2 \mu_B^2}{8\pi r_{jk}^3} (1 - 3 \cos^2 \theta_{jk}), \quad (3)$$

where the summations extend over all lattice sites; μ_0 , μ_B , h , and θ_{jk} represent the permeability of vacuum, the Bohr magneton, Planck's constant, and the angle between the applied magnetic field \mathbf{B} and the distance vector \mathbf{r}_{jk} interconnecting sites j and k , respectively.

To check the method for a 2D spin system, the M_4/M_2^2 -versus- f relationship has been calculated for $\mathbf{B} \parallel [111]$ with Eqs. (1)–(3) for a circular $(111)\text{Si}$ region enclosing $N = 1573$ Si atoms over which P_b defects ($S = \frac{1}{2}$)

are randomly distributed. The results are very similar to those of the 3D case.^{39,40} The ratio M_4/M_2^2 , which is generally used as a line-shape criterion,³⁸⁻⁴⁰ is a strong function of f : It is very large for small f but decreases strongly with increasing f ; $M_4/M_2^2 \rightarrow 3$ (the value of a Gaussian curve) for $f \rightarrow 1$.

The method of moments has repeatedly been applied to calculate linewidths³⁸⁻⁴¹ for the 3D case. Calculations on 3D crystals find in concert that for *high* f ($f > 0.1$) the linewidth is proportional to $f^{1/2}$, while M_4/M_2^2 is approximately, but not quite, 3. The shape is approximately Gaussian, although variations are seen both in linewidth and shape for different orientations of \mathbf{B} relative to the crystal due to the anisotropic nature of the DD interaction. More specifically, M_4/M_2^2 is generally in the range 2.1–2.6 for a simple cubic crystal.^{39,40} This ratio becomes very large ($M_4/M_2^2 \rightarrow +\infty$) for *dilute* systems, the linewidth now being proportional to f . This agrees quite well with experiment in high- f systems (see, e.g., Ref. 40) for which the line shape is observed to approach the Gaussian shape. As f decreases, the ratio M_4/M_2^2 increases, and the line shape tends to a more Lorentzian ($M_4/M_2^2 \equiv +\infty$) character. In between these limits the resonance line is mostly described as a Lorentzian with cutoff wings^{39,42} so that the ratio of moments matches theory.

Thus, the moment-versus- f relationships come out equal for the 2D and 3D cases. But, as a fundamental question, does this necessarily imply that the line shapes are identical? There is, as yet, no experimental answer to this question, as to our knowledge there has so far been no experimental report on the DD interactions between spins distributed over a single plane. More in-depth theoretical analysis, however, shows it is not. Using the local-field approximation as first worked out by Bloembergen, Purcell, and Pound,⁴³ Parker⁴¹ showed that the dipolar broadening of a $S = \frac{1}{2}$ system only leads to a Gaussian line shape if f is *sufficiently large*—compare with the $f > 0.1$ condition in Ref. 39—and if the spins are more or less *uniformly distributed* in space. This means that the basic condition for the dipolar broadening to generate a Gaussian line shape is thorough *averaging* of the spin-spin interactions in three dimensions. This only occurs if there are enough spins in each other's neighborhood— f has to be large—and if there are a lot of topologically different ways for the spins to be in each other's neighborhood, which increases strongly with the spin system's dimensionality. Hence why the 2D line shape may well differ from the 3D one. It has not to be Gaussian even if the ratio $M_4/M_2^2 \rightarrow 3$. Instead, lack of averaging in the missing third dimension may lead to much (partially) resolved fine structure, which statistics has failed to smear out. It is clear that the averaging will be particularly poor for the present 2D P_b system of low f .

The profound impact this has for a 2D spin system is nicely illustrated by extending Parker's calculations. Accordingly, we have calculated the dipolar histogram for a random P_b distribution of $f = 5 \times 10^{-3}$ at a (111)Si/SiO₂ interface using the local-field approximation. As an onset, we consider the interaction energy

$$E = \frac{\mu_0}{4\pi} \left[\frac{\boldsymbol{\mu}_j \cdot \boldsymbol{\mu}_k}{r_{jk}^3} - 3 \frac{(\boldsymbol{\mu}_j \cdot \mathbf{r}_{jk})(\boldsymbol{\mu}_k \cdot \mathbf{r}_{jk})}{r_{jk}^5} \right] \quad (4)$$

between two magnetic moments $\boldsymbol{\mu}_j$ and $\boldsymbol{\mu}_k$. This can be rewritten as

$$E = -\boldsymbol{\mu}_j \cdot \mathbf{B}_{jk}, \quad (5)$$

if defining

$$\mathbf{B}_{jk} = -\frac{\mu_0}{4\pi} \left[\frac{\boldsymbol{\mu}_k}{r_{jk}^3} - 3\mathbf{r}_{jk} \left[\frac{\boldsymbol{\mu}_k \cdot \mathbf{r}_{jk}}{r_{jk}^5} \right] \right] \quad (6)$$

as the magnetic field felt by $\boldsymbol{\mu}_j$ as a result of the presence of $\boldsymbol{\mu}_k$ at site k . If we substitute for the magnetic moments their quantum-mechanical analog $\boldsymbol{\mu} = g\mu_B \mathbf{S}$, the equations above transform into the DD interaction Hamiltonian [cf. Eq. (19)] which will be used in Sec. IV C. In general, the magnetic field \mathbf{B}_{jk} is dynamic, i.e., in an applied field \mathbf{B} all $\boldsymbol{\mu}_i$ will precess out of phase around \mathbf{B} . The polarization of $\boldsymbol{\mu}_k$ along \mathbf{B} makes up the static component, while the precessing motion induces a dynamic component perpendicular to \mathbf{B} . Spin flips and flip-flop transitions—the latter transitions result from the magnetic coupling of $\boldsymbol{\mu}_j$ and $\boldsymbol{\mu}_k$ via the dynamic magnetic fields they induce and are described by the second term in the full DD Hamiltonian [Eq. (22) in Sec. V]—account for the rest of the dynamic behavior. In the magnetostatic approximation of the local-field approach, all dynamic components are supposed to average out so that, apart from the applied field \mathbf{B} , the magnetic field at a given spin site is determined solely by the sum of the magnetic fields exerted *independently* by the other static spins (parallel to \mathbf{B}), i.e., the so-called *local field*. In this way, the resonance line shape is equivalent to the shape of the local-field distribution. As this model neglects spin flips (there is no rigorous theoretical justification for this magnetostatic approximation, certainly not in the case of identical spins), the calculated linewidth differs from the experimental one due to lifetime broadening and exchange-narrowing effects. The line shape, however, is a fair approximation, as has been shown by Parker for the 3D case.

For $\mathbf{B} \parallel [111]$, we may rewrite Eqs. (5) and (6) in the local-field approximation, using $\boldsymbol{\mu} = g\mu_B \mathbf{S}$, as

$$E = -\boldsymbol{\mu}_j \cdot \mathbf{B}_{jk}, \quad (7)$$

with

$$\mathbf{B}_{jk} = -\frac{\mu_0 g \mu_B}{8\pi r_{jk}^3} (1 - 3 \cos^2 \theta_{jk}). \quad (8)$$

In the exact quantum-mechanical calculation, the local field $B_{j,k}$ is given as

$$B_{jk} = -\frac{3}{2} \frac{\mu_0 g \mu_B}{8\pi r_{jk}^3} (1 - 3 \cos^2 \theta_{jk}). \quad (9)$$

The extra factor $\frac{3}{2}$ accounts for the Larmor precession-induced resonant coupling between like spins (spin-flip terms), which can only be computed quantum mechani-

cally.⁴⁴ The dipolar histogram for a random P_b distribution of $f = 5 \times 10^{-3}$ at a (111)Si/SiO₂ interface, calculated by means of Eq. (9) for a large number of randomly arranged spin distributions, is illustrated in Fig. 4. Fine-structure doublets are clearly resolved, the p th doublet resulting from the central spin- p th-neighbor spin interaction. It is obvious that this structure contributes significantly to the moments of the spectrum—even though the structure may not be very intense—and moment calculations will certainly overestimate the true linewidth if supposing a structureless line shape. On the other hand, this fine structure, which contributes to the signal intensity without increasing the linewidth (of the central line), will significantly increase the observed line-shape factor κ with increasing f , thus explaining the data in Fig. 2.

Because of the enhanced fine structure in a 2D spin system, it follows that Van Vleck's moment method is fundamentally unsuitable for exact calculation of dipolar effects, both as regards linewidth and line shape. This was well realized in previous moment-based calculations to investigate the P_b spin-spin interaction. Brower and Headley also found the moment method to be inadequate.²⁴ In their calculation, contributions of the resolved fine structure to the second moment were eliminated by excluding nearest-neighbor spin-pair interactions, up to the fifth neighbor. This approach appears realistic, as such pair interactions lead to resolved fine structure not contributing to the width of the central Zeeman resonance. While this procedure is possible for the second moment, it fails for the fourth. Hence, no information could be obtained on the line shape nor on its dependence on f . In an estimate, they used the adapted second-moment formula [Eq. (1)] to calculate the linewidth *assuming* a Gaussian line shape. This predicted

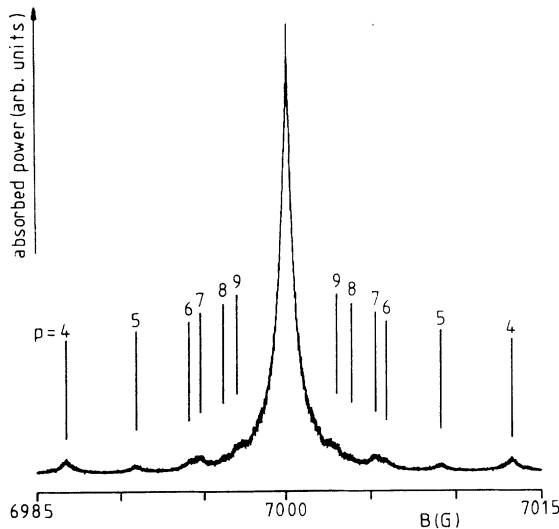


FIG. 4. Dipolar histogram of a 2D spin system ($S = \frac{1}{2}$) at a (111)Si surface. It is calculated for $\mathbf{B} \parallel [111]$ using the local-field approximation (see, e.g., Ref. 40) on a circular region containing $N = 1573$ Si atoms over which a fraction $f = 5 \times 10^{-3}$ of P_b spins are randomly distributed. The doublets p centered at the central line are fine structure arising from the p th nearest-neighbor pair dipolar interactions.

a dipolar contribution of 2.6 G to the absorption linewidth for $f \approx 5 \times 10^{-3}$. In a somewhat different statistical approach, Braet and Stesmans²⁵ carried out moment calculations assuming a cutoff Lorentzian line shape. For $f = 8.6 \times 10^{-3}$ they found a dipolar absorption width of 24.5 G. When excluding first and both first and second neighbors (also out of M_4), they obtained dipolar linewidths of 8.5 and 5.9 G, respectively, thereby showing the importance of nearby spins on the moments and linewidths. When excluding first and second neighbors, the value $\Delta B = 3.7$ G was calculated for $f = 5.3 \times 10^{-3}$. Clearly, the estimates of both calculations are far too high as compared to the data in Fig. 2.

It follows that the method of moments is inappropriate to calculate the dipolar broadening of the P_b resonance. Even worse is that it fails totally to provide information on the line shape of a 2D interacting spin system. The overestimation on the linewidth, as calculated from M_2 , just results from the fact that *the correct line shape is not taken into account*. Instead, an overall, structureless shape, i.e., Gaussian or truncated Lorentzian, lacking the typical structure exposed by a 2D spin system, is just *assumed*.

2. Saturation data

Using the Bloch theory and assuming adiabatic slow passage conditions, the absorption susceptibility χ'' of a resonance line versus microwave frequency, containing both homogeneous and inhomogeneous broadening, can be written as³⁷

$$\chi''(\omega) = \frac{1}{2} \chi_0 \int_0^{+\infty} \frac{\pi \omega' g(\omega - \omega') h(\omega' - \omega_0)}{1 + \pi \gamma^2 B_1^2 T_1 g(\omega - \omega')} d\omega', \quad (10)$$

where χ_0 , γ , B_1 , T_1 , and $\omega_0 = \gamma B_0$ represent the static susceptibility, the gyromagnetic ratio, the amplitude of the circularly polarized microwave field at the sample site, the spin-lattice relaxation time, and the central angular resonance frequency, respectively. The homogeneous and inhomogeneous line shapes are represented by $g(\omega)$ and $h(\omega)$, respectively. For the case where the homogeneous part is described by a Lorentzian curve and the inhomogeneous part by a Gaussian, Castner³⁷ calculated that the susceptibility at the center of the absorption line (proportional to the signal amplitude) can be written as

$$\chi'' = \chi_0 \sqrt{\pi \ln 2} \frac{B_0}{\Delta B_G} \frac{e^{a^2 t^2}}{t} [1 - \Phi(at)], \quad (11)$$

where $a \equiv \sqrt{\ln 2} \Delta B_L / \Delta B_G$ is $\sqrt{\ln 2}$ times the ratio of the homogeneous (spin packet) and inhomogeneous absorption linewidths, $t \equiv (1 + \gamma^2 B_1^2 T_1 T_2)^{1/2}$ is the saturation factor, T_2 is the transverse relaxation time, and Φ is the error function. As the ratio of the susceptibility (intensity) of the investigated resonance line and a susceptibility marker can be measured quite accurately in their respective line centers, Eq. (11) enables us to determine the linewidth ratio a and the saturation factor t . Both quantities provide important information on the spin dynamics.

Braet and Stesmans^{22,36} used ESR measurements at different microwave frequencies to deconvolve the P_b sig-

nal (for $[P_b] \approx 5 \times 10^{12} \text{ cm}^{-2}$) in frequency-dependent and frequency-independent parts; the former part is of inhomogeneous nature, as it is due to a (Gaussian) g distribution. The frequency-independent part, which dominates the total linewidth, was assumed to be homogeneous and of Lorentzian shape, leading in this way to the variables ΔB_L and ΔB_G (and a). At a fixed frequency (ΔB_G constant) and temperature ($T_1 T_2$ constant), a and t were determined by fitting Eq. (11) to the continuous-wave saturation plot—that is, the derivative signal height V_D (or the relative height times B_1 if measuring relative to a nonsaturating standard) versus B_1 —and correcting for the fact that the first derivative of the absorption instead of the absorption signal was measured (see, e.g., Ref. 36). This led to confident values for t and ΔB_L , as indeed the fitting quality was satisfying, indicating that the assumption of the homogeneous character of the frequency-independent broadening was correct. The inferred a value was consistent with the one deduced from self-consistent fitting of the frequency-dependent Pb signal.²² This enabled the calculation of T_1 and the spin-spin relaxation time T_2^* in the range $T=2.4\text{--}25$ K. For this, $T_1 T_2$ was extracted from t and compared to the spin-packet width, which is given as $\Delta B_L \equiv 2/(\gamma T_2)$ for a Lorentz curve (see Ref. 36 for detailed information). As $1/T_2 = 1/T_2^* + 1/T_1$ and because T_2 was much shorter than $\sqrt{T_1 T_2}$, they argued that in a good approximation $T_2^* = T_2$. This suggests that the spin-packet width ΔB_L , which is of the order of the measured linewidth ΔB , is determined exclusively by spin-spin interactions, i.e., homogeneous dipolar broadening. This conclusion agrees with the T dependence of the P_b signal width for good quality (111)Si/SiO₂. Indeed, if instead of $T_2 \ll T_1$ one would have $T_2 \approx T_1$ (negligible spin-spin interaction), the homogeneous linewidth, and thus also the total linewidth, would show a T -dependent broadening, which is not observed.²²

On the other hand, if the frequency-independent linewidth would be predominantly of inhomogeneous character (e.g., unresolved hyperfine broadening), it would have been impossible to fit the saturation data consistently with Eq. (11) using the value of a as obtained from the frequency-dependent measurements.^{22,36} So, in accordance with the moment calculations, saturation theory points to a considerable dipolar line broadening. Later on, the same saturation⁴⁵ characteristics were found on distinctly differently grown (111)Si/SiO₂ structures (native oxide). Some saturation plots were also obtained by Carlos⁴⁶ for P_b defects in SIMOX (separation by implanted oxygen) structures. In this work, however, the role of the DD interactions was not recognized.

There are some factors that make the quantitative determination of a , and thus of the dipolar broadening, less accurate. First, beside the frequency-independent dipolar broadening, there has to be admixing of another frequency-independent inhomogeneous broadening due to unresolved hyperfine interactions. From the literature on deep defects in silicon (see, e.g., Refs. 47 and 48), this broadening is known to be non-negligible. Second, the Lorentzian and Gaussian line shapes, used in Castner's

saturation theory³⁷ for the homogeneous and inhomogeneous broadening, respectively, may not be very good approximations. As outlined above, local-field calculations show that the description of the (homogeneous) dipolar broadening by a Lorentz curve is mostly incorrect—particularly for the 2D case. As regards the (inhomogeneous) hyperfine broadening of the P_b signal, evidence against a Gaussian shape for this broadening will be presented in Sec. IV B. Third, even if experiments were accurate and theory were correct, it would still be difficult to determine accurate values of a , as the saturation plot appears rather insensitive to small variations in a .

The dipolar origin of the concentration-dependent line broadening depicted in Fig. 2 can be ascertained from saturation analysis. Therefore, we measured saturation plots as a function of $[P_b]$ on sample S1. If, as claimed, the concentration-dependent linewidth broadening is due to DD broadening, the parameter $a = \sqrt{\ln 2} \Delta B_L / \Delta B_G$ should increase with increasing spin concentration due to the growth of ΔB_L . But, instead, should it originate from a change in interface strain—there are reports in the literature suggesting that post-oxidation annealings can fundamentally change the interface structure in a way different from nitridation, oxidation or (de)hydrogenation— a would stay constant or decrease with increasing f , depending on the amount of strain broadening (g distribution). Saturation plots for two different concentrations are superposed in Fig. 5. The dotted and dashed lines represent the completely homogeneous ($a = +\infty$) and inhomogeneous ($a = 0$) saturation curves, respectively, as calculated from Castner's theory³⁷ for the $dP_{\mu a}/dB$ signals. The square and diamond symbols are the P_b data for concentrations of $(55 \pm 4) \times 10^{11}$ and $(121 \pm 6) \times 10^{11} \text{ cm}^{-2}$, respectively. Both saturation plots clearly indicate that the P_b resonance contains a dominant homogeneous (Lorentzian) component. Moreover, the fact that, after reaching a maximum value, the higher- f saturation curve (diamonds) bends down earlier than the lower- f data (squares) shows that the higher- f P_b resonance has a higher a value. This necessarily means that the P_b signal gets increasingly more homogeneous (increasing ΔB_L) with growing density, as expected for a signal broadened by DD interactions. The alternative, that is, ascribing it to a decrease in ΔB_G , i.e., a reduction of strain broadening, is untenable. It would conflict with the overall increase in P_b linewidth with increasing f . Saturation curves for other f values corroborate this behavior.

It has been reported previously²⁰ that the spin-lattice relaxation time of P_b centers, and hence the saturability, increases significantly with increasing hydrogenation.²⁰ This was tentatively ascribed to a variation in the phonon density of states of the oxide by the annealing in hydrogen. As a phonon bottleneck effect may be excluded,⁴⁹ this implies that the intrinsic spin-phonon relaxation of the P_b center would be dominated by its coupling to the oxide side of the interface. Within experimental scatter—due, for instance, to a change in cavity Q or cavity coupling between different sample mountings—we

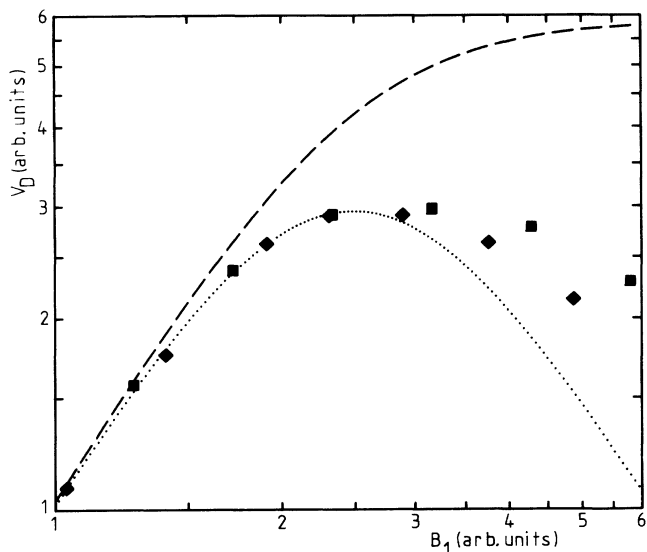


FIG. 5. Saturation plot, that is, ESR absorption-derivative signal amplitude V_D vs B_1 , of P_b centers at the (111)Si/SiO₂ interface for two P_b densities: $(55 \pm 4) \times 10^{11} \text{ cm}^{-2}$ (■) and $(121 \pm 6) \times 10^{11} \text{ cm}^{-2}$ (◆). The dotted and dashed curves represent theoretical variations for the extreme cases of purely homogeneously and inhomogeneously broadened spin systems, respectively. The more homogeneous character of the higher-concentration sample is clearly revealed. Measurements were carried out for $\mathbf{B} \parallel [111]$ at $T = 6 \text{ K}$ and 20.2 GHz . The two data sets were matched to each other at maximum V_D values.

did not observe any such systematic increase of T_1 . Yet we do see systematic variations in saturability with increasing hydrogenation (decreasing $[P_b]$): saturability is enhanced as f decreases. Saturation measurements on one sample, however, show that the amount of change is well explained by the increase in T_2 —not T_1 —resulting from the receding DD broadening as f decreases.

Along one interpretation, one might suggest that these contrasting findings relate to differences in initial oxide quality (structure), e.g., variations in the positive fixed charge near the interface, resulting from unequal growth procedures. The impact of hydrogenation may then be different. For instance, a modification by hydrogenation of the positive fixed charge, which can create a conduction electron bath (a very efficient relaxation path⁴⁵) at the interface, might significantly alter T_1 .

B. The residual P_b resonance line shape ($f \rightarrow 0$) for $\mathbf{B} \parallel [111]$

Figure 2 shows that in absence of any dipolar line broadening ($f \rightarrow 0$), the residual derivative linewidth of the P_b signal is given as $\Delta B_{pp}^R = 1.29 \pm 0.03 \text{ G}$, while the line shape is characterized by $\kappa = 2.0 \pm 0.1$. Saturation measurements have demonstrated that this large a linewidth cannot be ascribed to T_1 lifetime broadening nor to strain broadening. In support, frequency-dependent ESR observations^{22,36} provide a direct proof for the latter. Moreover, calculation of the dangling-bond \vec{g} dyadic by Watkins and Corbett⁴⁷ show that strain broadening in g_{\parallel} vanishes to first order. This leaves as the most plausible explanation for the residual linewidth

the idea that it results from unresolved hyperfine interactions of the unpaired defect electron²³ with neighboring ²⁹Si and eventually ¹⁷O nuclei¹⁰ $I = \frac{5}{2}$. The observation of a superhyperfine doublet^{10,11,13} supports this assignment, and indicates that the spectrum is not exchange narrowed, as suggested before.²³ For unenriched oxides with a natural abundance of ¹⁷O of 0.037%, the contribution of ¹⁷O hyperfine interaction to the linewidth can be neglected.⁵⁰

Accepting then that the residual P_b signal is dominated by (partially) unresolved ²⁹Si hf splittings, what is the expected line shape for the 2D spin system? Among others, it should explain the measured line-shape factor $\kappa = 2.0 \pm 0.1$. If we want to calculate the theoretical line shape of the P_b defect at higher f , where the DD interactions come into play, the knowledge of the residual line shape ($f \rightarrow 0$) will be necessary. In this respect, it is instructive to examine similar line shapes for other paramagnetic centers in Si, for which unresolved hf broadening is the dominant line-broadening mechanism, too.

With this approach, Brower²³ pointed to an ESR study by Feher⁵¹ of donors in natural and ²⁸Si-enriched *c*-Si showing that unresolved hf interactions between the donor electron and ²⁹Si nuclei dominate the donor resonance linewidth and shape. The M_4/M_2^2 ratio of all donor lines was found to approach the characteristic value 3 of a Gaussian curve, the deviations getting smaller as the donor-electron ionization energy becomes smaller. In this work, a semiempirical calculation of the line shape was also carried out using experimental values for the hf splittings obtained by electron nuclear double resonance (ENDOR) and theoretical estimates calculated from the Luttinger and Kohn donor wave function.⁵² This calculation predicted a closely Gaussian shape for the donor line shape, in agreement with observations. However, the line shape starts to deviate from its predicted profile when the number of nuclear spins with which the donor electron may interact is decreased. This may be achieved either by a ²⁸Si enrichment or by a larger donor-electron ionization energy, which reduces the electron wave-function extension. As the P_b center is a dangling-bond-like deep defect as well, the residual P_b line shape in unenriched SiO₂/Si ($[^{29}\text{Si}] \approx 4.70\%$) is expected to exhibit similar characteristics, which, because of their hf origin, are independent of $[P_b]$.

The same conclusion can be reached from adapting Parker's local-field calculations towards the hf interaction. Instead of the electron-spin–electron-spin interaction, which determines the DD broadening, the hf interaction deals with electron-spin–nuclear-spin interaction, which is a similar physical situation. One difference, though, with the calculations originally carried out by Parker is that the gyromagnetic ratios of the respective spins in the case of the hf interaction are quite different. This implies that there can be no resonant coupling between their precession motions, thereby strongly diminishing the importance of flip-flop terms in the dipolar hf Hamiltonian. This makes the magnetostatic approximation in the local-field calculations even more plausible than in the case of the successful calcula-

tions by Parker.⁴¹ As mentioned, it has been well shown within the local-field model⁴¹ that the spin-spin interactions only lead to a Gaussian profile if the number of nuclear spins interacting with the electron spins is sufficiently high. The local-field model thus predicts that the resulting profile is Gaussian, provided that the hf interaction is sufficiently averaged.

Having ascertained the importance of the hf broadening and a qualitative understanding of the P_b hf profile, it remains to obtain an analytical description of the hf profile. In a first empirical (crude) approach, the line shape can be simulated by a symmetrical sum of Gaussian profiles, positioned near the center of the resultant shape. The constituent Gaussian shape will perhaps not be correct in general, but it does not matter to first order. This procedure should allow us to obtain a good approximation of the central line shape as well as of the resolved structure, which would suffice to serve as residual line shape when investigating the dipolar changes of the line shape with increasing f (see Sec. IV C), though it leads to little physical insight. Along this approach we calculated a residual line shape, called residual spectrum R1, by simply summing five Gaussian lines, characterized by the derivative linewidths ΔB_{pp}^i and relative intensities I_i , centered at the ^{28}Si P_b resonance field and two Gaussian profiles (each characterized by $\Delta B_{pp}^{\text{shf}}$ and I_{shf}) shifted over $\pm A_{\parallel}^{\text{shf}}/2$ to simulate superhyperfine signals. This residual spectrum R1 is shown in Fig. 6 together with the experimental line shape to which it is fitted. The fitting values are tabulated in Table I.

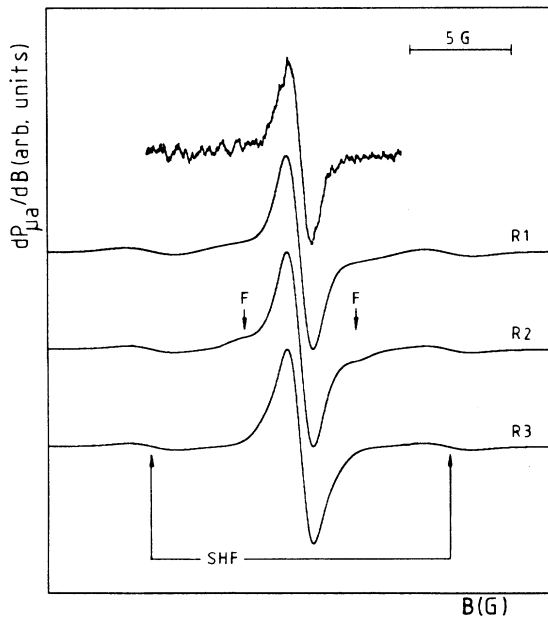


FIG. 6. The experimental K -band P_b residual line shape (top spectrum; $f \approx 3 \times 10^{-4}$), measured at 4.3 K for $\mathbf{B} \parallel [111]$ together with three calculated residual line shapes: R1, sum of Gaussian curves; R2, parametrized cluster calculation; R3, based on the $\text{Si}_{22}\text{H}_{27}$ P_b cluster calculation (Ref. 13). Though the experimental curve does not show any clear resolved structure (positions F) probably due to the low S/N ratio, the best fits are obtained by spectra R1 and R2 (see also Table I).

TABLE I. Theoretical simulations of the residual ESR line shape of the [111] P_b center at the (111)Si/SiO₂ interface for $\mathbf{B} \parallel [111]$, compared with experimental data. Model R1 represents a simple summation of Gaussian lines where ΔB_{pp}^i and I_i symbolize the peak-to-peak linewidths and relative intensities, respectively; $A_{\parallel}^{\text{shf}}$ represents the superhyperfine splitting (see Refs. 11–13). Model R3 is based on a $\text{Si}_{22}\text{H}_{27}$ P_b cluster calculation as presented in Ref. 13, while model R2 is an adapted version of model R3 to optimize the fit to experimental data. The number of equivalent Si atoms and corresponding hyperfine splitting in each shell i are given by k_i and A_{\parallel}^i , respectively. ΔB_{pp}^C is the peak-to-peak linewidth of the Gaussian curve used to convolute the histograms of model R2 and R3.

Model	I_1 ΔB_{pp}^1 (G)	I_2 ΔB_{pp}^2 (G)	I_3 ΔB_{pp}^3 (G)	I_4 ΔB_{pp}^4 (G)	I_5 ΔB_{pp}^5 (G)	I_{shf} $\Delta B_{pp}^{\text{shf}}$ (G)	k_1 A_{\parallel}^1 (G)	k_2 A_{\parallel}^2 (G)	k_3 A_{\parallel}^3 (G)	k_4 A_{\parallel}^4 (G)	k_5 A_{\parallel}^5 (G)	k_6 A_{\parallel}^6 (G)	$A_{\parallel}^{\text{shf}}$ (G)	ΔB_{pp}^C (G)	ΔB_{pp}^R (G)	ΔB_{pp}^R (G)	κ
R1	0.074 1.00	0.295 1.42	0.030 1.85	0.061 2.60	0.540 4.90	0.0735 2.70							14.6		2.00	1.284	3.03
R2							3 2.1 3	3 14.8 3	6 1.0 6	3 4.8 3	3 1.9 3	3 2.9 3		1.19	1.92	1.287	2.47
R3 ^a							1.07 ^b	14.8 ^c	1.91	2.82	0.99	1.24		1.11	1.86	1.285	2.09
Expt.													14.8		1.98	1.29	2.0

^aCalculated using the absolute isotropic hf interaction constants (Fermi-contact splitting a) as given for the relaxed $\text{Si}_{22}\text{H}_{27}$ P_b cluster in Ref. 13.

^bValue of A_{\parallel} containing both the isotropic and anisotropic hf interaction.

^cThe experimental shf splitting has been used instead of the theoretical value to enhance accuracy.

A second, more refined approach consists of considering a cluster of atoms surrounding a P_b center and calculating the hf histogram using the statistical expressions describing the hf interactions of the unpaired electron with the ^{29}Si nuclei for the different configurations (^{29}Si occupancies) of the cluster. The particular hf splittings pertaining to each Si shell are the parameters in this model. By selecting an adequate broadening function, it should be possible with such a semiempirical parametrized model to test the theoretical hyperfine splittings predicted by Cook and White.¹³ The model will also allow one to take into account the fact that the hyperfine splittings are quite sensitive to changes in the defect symmetry and interface strain⁹ (change in the hybridization of the electron wave function).

In the semiempirical parametrized model, let K be the total number of Si sites at which the P_b wave function has a non-negligible probability density. These sites can be subdivided into β shells along symmetry and distance towards the central atom, where each shell α contains k_α Si atoms of which q_α are ^{29}Si isotopes. All ^{29}Si spins within a shell are assumed to be equivalent as regards the hf interaction. Let Q be the total number of ^{29}Si nuclei involved. The probability that a Si atom is a ^{29}Si isotope equals the natural abundance $\xi=0.047$. The probability for a shell α to contain q_α ^{29}Si atoms on k_α possible sites is described by the binomial distribution. As $Q = \sum_{\alpha=1}^{\beta} q_\alpha$ and $K = \sum_{\alpha=1}^{\beta} k_\alpha$, the probability for the defect cluster to contain Q ^{29}Si isotopes, subdivided along the different shells as described by one set of q_α 's, can be written as

$$P(\xi; q_1, \dots, q_\beta; k_1, \dots, k_\beta) = \xi^Q (1-\xi)^{K-Q} \prod_{\alpha=1}^{\beta} \frac{k_\alpha!}{q_\alpha! (k_\alpha - q_\alpha)!} \quad (12)$$

The normalized intensity $I_\alpha(x_\alpha, q_\alpha)$ of each hyperfine line x_α within a multiplet, built up by the q_α ^{29}Si nuclei of shell α , equals

$$I_\alpha(x_\alpha, q_\alpha) = \frac{q_\alpha!}{x_\alpha! (q_\alpha - x_\alpha)! 2^{q_\alpha}} \quad (13)$$

where x_α is the index running over the different $(2q_\alpha I + 1 = q_\alpha + 1)$ spectral lines of the multiplet. The intensity of one hf line in the ultimate stick diagram of the P_b electron, delocalized over the K Si atoms of the cluster, can be easily calculated from Eqs. (12) and (13) as

$$I(\xi; x_1, \dots, x_\beta; q_1, \dots, q_\beta; k_1, \dots, k_\beta) = \frac{\xi^Q (1-\xi)^{K-Q}}{2^Q} \prod_{\alpha=1}^{\beta} \frac{k_\alpha!}{x_\alpha! (q_\alpha - x_\alpha)! (k_\alpha - q_\alpha)!} \quad (14)$$

For $\mathbf{B} \parallel [111]$, the final stick diagram is obtained by assigning the correct resonance field to each hf line and summing over all $x_\alpha = 0, \dots, q_\alpha$ and $q_\alpha = 0, \dots, k_\alpha$ allowed. The magnetic-field shift of the hyperfine line $I(\xi; x_1, \dots, x_\beta; q_1, \dots, q_\beta; k_1, \dots, k_\beta)$ relative to the center of the spectrum [the ^{28}Si ($I=0$) and ^{30}Si ($I=0$) P_b resonance field] is

$$\delta B(x_1, \dots, x_\beta; q_1, \dots, q_\beta; A_{\parallel 1}, \dots, A_{\parallel \beta}) = \sum_{\alpha=1}^{\beta} \left[x_\alpha - \frac{q_\alpha}{2} \right] A_{\parallel \alpha} \quad (15)$$

where $A_{\parallel \alpha}$ is the hyperfine tensor value along $[111]$ in field units for ^{29}Si atoms in shell α . Equations (14) and (15) lead to the total hyperfine stick diagram. Finally, the hyperfine line shape is obtained by convoluting the stick diagram with a broadening function (of derivative linewidth ΔB_{pp}^C) for which the Gaussian profile has been taken. This profile is chosen to represent the hyperfine interaction with distant ^{29}Si nuclei that have not been taken into account in the explicit hyperfine calculation above.

Up to now we did not include in the calculation a possible distribution of $A_{\parallel \alpha}$ resulting from the dependence of the P_b wave-function hybridization parameters on the interface strain. This is easily done by replacing each $A_{\parallel \alpha}$ in Eq. (15) by a Gaussian distribution with a standard deviation σ_α such that

$$\sigma_\alpha = c A_{\parallel \alpha} \quad (16)$$

for all α . c can be calculated by fitting the model to the experimentally observed hf and shf linewidths of the P_b resonance,⁹ giving $c = 0.11 \pm 0.03$. As the value for c is rather small, the distribution in A_α can safely be neglected for the calculation of the central line shape. The number of Si shells is taken as $\beta=6$ in the calculations.

Two residual line shapes, labeled as residual spectra $R2$ and $R3$ in Fig. 6, were calculated using the semiempirical model described by Eqs. (14) and (15). The parameters used can be found in Table I, together with some data on the experimental residual spectrum. Residual spectrum $R3$ is obtained using the hyperfine parameters $A_{\parallel \alpha}$, incorporating both isotropic and anisotropic hf interaction, insofar as specified by Cook and White¹³ from calculations on a relaxed $\text{Si}_{22}\text{H}_{27}$ P_b cluster model. The other hyperfine parameters were set equal to the respective (isotropic) Fermi-contact splittings a , given in their Table III (see Ref. 13). For the superhyperfine splitting we used our experimental result (i.e., $A_{\parallel} = 14.8$ G; see below) in order to enhance accuracy. Model $R2$ is an adapted version of spectrum $R3$ as to optimize the fit to the residual experimental curve.

It remains to select the spectrum out of the three calculated that conforms best to the experiment and will be used in the next section to convolute the dipolar histograms. The partially resolved hyperfine structure close to the central line (positions F), typical for deep-level defects in silicon, is clearly seen in spectra $R1$ and $R2$ in Fig. 6. This structure is somewhat blurred in spectrum $R3$, calculated using the Cook and White parameters. In the experimental residual spectrum, no resolved structure is seen. However, this is believed to result mainly from the unavoidably low S/N ratio of the spectrum. Anyhow, comparison by eye of the different residual spectra does not allow us to prefer one above the other; the final arbiter will be the success of their use in convoluting dipolar histograms so as to produce correct dipolar line shapes (Sec. IV C). Yet the comparison in Table I may

give some indication. As regards κ , it is clearly seen that the values of the theoretical line shape are all higher than the experimental one. This may partly be due to the low S/N ratio of the $f \rightarrow 0$ experimental signal, which makes the determination of κ less accurate. However, this error is likely very small, as the experimental κ values for low and high f match fluently (see Fig. 2). The κ of spectrum $R1$ comes out highest, while the other two agree reasonably well with experiment. The comment regarding ΔB_{pp}^R is short: all three approach the experimental value very closely. This should not come as a surprise, since the different theoretical spectra were optimized (cf. ΔB_{pp}^i and ΔB_{pp}^c in Table I) so as to match the experimental ΔB_{pp}^R value. This optimization as regards the experimental ΔB_{pp}^R value for all three models implies that the model "inadequacies" will show up as differences in ΔB^R . In this respect, spectrum $R3$ (the $\text{Si}_{22}\text{H}_{27}$ model) appears the least correct. But, as mentioned, we will continue to use all three residual line shapes in the calculation of the dipolar P_b line shape (Sec. V); a final selection will follow.

C. Dipolar interaction in the P_b signal for $\mathbf{B} \parallel [111]$; fine structure

The spin Hamiltonian of n spins in a static field \mathbf{B} can be written as (see, e.g., Ref. 53)

$$\mathcal{H} = \mu_B \sum_{i=1}^n \mathbf{B} \cdot \vec{g}_i \cdot \mathbf{S}_i + \sum_{\substack{i,j \\ (i < j)}} \mathbf{S}_i \cdot \vec{K}_{ij} \cdot \mathbf{S}_j, \quad (17)$$

with \vec{g}_i the g tensor of spin i and \vec{K}_{ij} the tensor describing the spin-spin interaction between spins i and j . Deviations of the P_b g tensor elements from the free-electron g value (g_0) are small, since the spin-orbit coupling in Si is small compared to the crystal-field splitting of the orbital states, and the P_b ground state is an orbital singlet (Kramer's doublet). Moreover, the g dyadic is approximately the same for all P_b defects at the (111)Si/SiO₂ interface—especially g_{\parallel} [$\mathbf{B} \parallel [111]$, perpendicular to the (111) interface]—so that the subscript i of the g tensor in Eq. (17) can be dropped for the present case.

Generally, \vec{K}_{ij} can be subdivided into

$$\mathbf{S}_i \cdot \vec{K}_{ij} \cdot \mathbf{S}_j = J_{ij} \mathbf{S}_i \cdot \mathbf{S}_j + \mathbf{S}_i \cdot \vec{D}_{ij} \cdot \mathbf{S}_j + \mathbf{S}_i \cdot \vec{N}_{ij} \cdot \mathbf{S}_j, \quad (18)$$

with $J_{ij} = \text{Tr}(\vec{K}_{ij})/3$, \vec{D}_{ij} a symmetrical tensor satisfying $\text{Tr}(\vec{D}_{ij}) = 0$ and \vec{N}_{ij} an antisymmetrical tensor with, of course, $\text{Tr}(\vec{N}_{ij}) = 0$. The first term on the right-hand side of Eq. (18) describes the isotropic exchange interaction with interaction coefficient J_{ij} while the other two right-hand-side terms describe anisotropic interactions. This interaction actually contains two parts, i.e., direct exchange and superexchange⁵⁴ with interaction coefficients J'_{ij} and J''_{ij} , respectively, so that $J_{ij} = J'_{ij} + J''_{ij}$. The sign of J_{ij} determines whether the interacting spins i and j are in a triplet (negative sign) or a singlet (positive sign) ground state. The tensor \vec{D}_{ij} contains the symmetrical part of

the dipole-dipole and superexchange interactions, while \vec{N}_{ij} stands for the antisymmetrical part of both interactions. The antisymmetrical part of the DD interaction comes in due to the anisotropy of the interacting magnetic moments (cf. the \vec{g} dyadic) and is generally much smaller than the symmetrical part⁵³ when $\Delta g = g - g_0 \ll g$.

Various simplifications apply^{24,53,55,56} for the studied dilute (typically $f \approx 5 \times 10^{-3}$) magnetic system composed of identical spins with $S = \frac{1}{2}$. The result is that, first, we may neglect the contribution of exchange and superexchange interactions to the spin-spin interaction Hamiltonian, and, second, the DD interaction can be described by a symmetric tensor (\vec{D}) only. Hence, the spin-spin interaction Hamiltonian is approximated solely by the DD interaction between pure spin states⁵⁷ so that

$$\mathbf{S}_i \cdot \vec{K}_{ij} \cdot \mathbf{S}_j = \frac{\mu_0 g^2 \mu_B^2}{4\pi} \left\langle \frac{\mathbf{S}_i \cdot \mathbf{S}_j}{r_{ij}^3} - 3 \frac{(\mathbf{S}_i \cdot \mathbf{r}_{ij})(\mathbf{S}_j \cdot \mathbf{r}_{ij})}{r_{ij}^5} \right\rangle. \quad (19)$$

The brackets in Eq. (19) indicate the averaging of r_{ij} over the wave functions of spins i and j . If the spin-spin distance r_{ij} is much larger than the wave-function delocalizations, as discussed, then the spatial part of the wave functions of the unpaired defect electrons may be replaced by δ functions, i.e., the so-called *point-dipole approximation*.²⁴ In the case of very close spins, DD fine-structure splittings should be calculated using a linear combination of Slater $3s, 3p$ atomic orbitals for the P_b wave function, taking, for instance, the orbital population coefficients calculated by Cook and White.¹³ At these distances, however, the DD interaction is not the only significant interaction involved, making the enhanced accuracy on the DD interaction of little value. It can be concluded that the above approximations will be inadequate for the case where the resulting line shape will exhibit much resolved fine structure of substantial splitting. On the contrary, the approximations are reliable when the central line dominates the ESR spectrum, as can be inferred, for instance, from local-field calculations.

As \mathbf{B} is tilted away from the [111] direction towards the interface plane, the linewidth and shape of the P_b signal get increasingly more dominated by strain broadening,^{23,28} thus masking the influence of other line-broadening mechanisms. This is a main reason why we will calculate the dipolar contribution only for $\mathbf{B} \parallel [111]$. Another reason is that the S/N ratio is best for this field orientation, which is of prime importance when looking for weak and/or partly resolved structure on the resonance.

The basic calculation scheme⁵⁸ is then similar to that of Ref. 24. We choose a Cartesian coordinate system with $\mathbf{z} \parallel [111]$ and $\mathbf{x} \parallel [11\bar{2}]$. All P_b sites are considered lying in the x, y plane and we define ϕ_{ij} as the angle between \mathbf{x} and \mathbf{r}_{ij} . Then the spin-Hamiltonian operator can be written as

$$\mathcal{H} = g_{\parallel} \mu_B \mathbf{B} \sum_{i=1}^n S_{z_i} + \frac{\mu_0 g^2 \mu_B^2}{16\pi} \sum_{\substack{i,j \\ (i < j)}} \left[4 \frac{S_{z_i} S_{z_j}}{r_{ij}^3} - \frac{S_i^+ S_j^- + S_i^- S_j^+}{r_{ij}^3} - 3 \frac{S_i^+ S_j^+ e^{-2i\phi_{ij}} + S_i^- S_j^- e^{2i\phi_{ij}}}{r_{ij}^3} \right]. \quad (20)$$

As a basis for the spin wave function of a system of n spins, we choose the $|S_1 \cdots S_n; M_1 \cdots M_n\rangle$ states, with $S_i = \frac{1}{2}$ for all i and with two possible values for each magnetic quantum number M_i ($\pm \frac{1}{2}$)— 2^n states all together. The 2^n energy levels E_i and eigenstates, denoted by $|i\rangle$, are obtained by numerically solving the eigenvalue equation from which the transition energies $\Delta E_{kl} = |E_k - E_l|$ and transition probabilities P_{kl} are calculated.²⁴ The transition probabilities are normalized so that the total absorption matches the number of spins $\sum_{k,l=1}^n P_{k,l} = n$. Other dependences of the absorption, for instance on the microwave field strength, are not taken into account, as they are not relevant for the present purpose. All calculations were performed with an IBM 3090/400e VF mainframe using a FORTRAN program. The n -spin dipolar histogram (stick diagram)—this is the intensities of the resonance transitions of the n DD-interacting spins versus the magnetic field—calculated along this scheme is stored in a computer array with a resolution of 200 data points (sticks)/G.

For the practical calculations, we consider a circular region of diameter d in an unreconstructed (111)Si plane enclosing N Si atoms, over which are distributed n P_b spins. Part of this region is illustrated in Fig. 7, where the nearest neighbors to the central Si atom are identified by circles. The Si sites form a 2D triangular net of lattice parameter $a_L = 3.8426$ Å. However, as it is not necessarily so that all Si sites in a (111) plane may be the center of a P_b defect, but perhaps only a subset of these sites, we will call from now on the subset of Si sites on which P_b defects may be located a *net* or *array*. It is a main aim of this work to draw conclusions about the particular array of allowed sites for the P_b centers, and calculations have been carried out for various nets. The P_b centers are assumed to be *randomly distributed* over the net unless stated otherwise. In the extreme case where the array

comprises all Si-atom sites in a (111) plane—the most general net—it is referred to as the *random-distribution model*.

The calculation procedure for a given measured fractional site occupancy f of P_b centers at the (111)Si/SiO₂ interface and a supposed P_b distribution model (array) consists of the following steps. First, the average number of P_b defects $\bar{n} = fN$ occurring in the circular region of the net comprising N Si sites is calculated, of which N_{al} are allowed P_b sites, and the array (net) fractional site occupancy $f' = f(N/N_{al})$. Clearly, for the case of the random-distribution model, $N_{al} = N$ and $f' = f$. As the distribution of defects over the net is random, the number of P_b defects within equally sized confined regions of the interface is not always exactly \bar{n} but may fluctuate between $n=0$ and $n=N_{al}$. In order to get theoretical results that represent a macroscopic (111)Si/SiO₂ interface (as experimentally studied), we calculate in a second step the n -spin dipolar histograms $I_n(\mathbf{B}, N_{al})$ for n ranging from 1 to n_{max} ; the value of n_{max} will be determined below. Each such n -spin histogram is calculated as an average over all possible, or else a great number of, random configurations of n spins over N_{al} net sites. This leaves us with n_{max} dipolar histograms, of which each has thus been averaged with respect to fluctuations over the (111)Si/SiO₂ interface. In a third step, the dipolar histograms are subsequently added together in proportion to their statistical probability of occurrence $P(N_{al}, n, f') = \{N_{al}! / [n!(N_{al} - n)!]\} f'^n (1 - f')^{N_{al} - n}$, composing in this way the total dipolar histogram $I(f', \mathbf{B}, N_{al})$ as

$$I(f', \mathbf{B}, N_{al}) = \sum_{n=1}^{n_{max}} P(N_{al}, n, f') I_n(\mathbf{B}, N_{al}). \quad (21)$$

In a fourth, final step, the total dipolar histogram is convoluted with a residual line shape (see Sec. IV B) to ac-

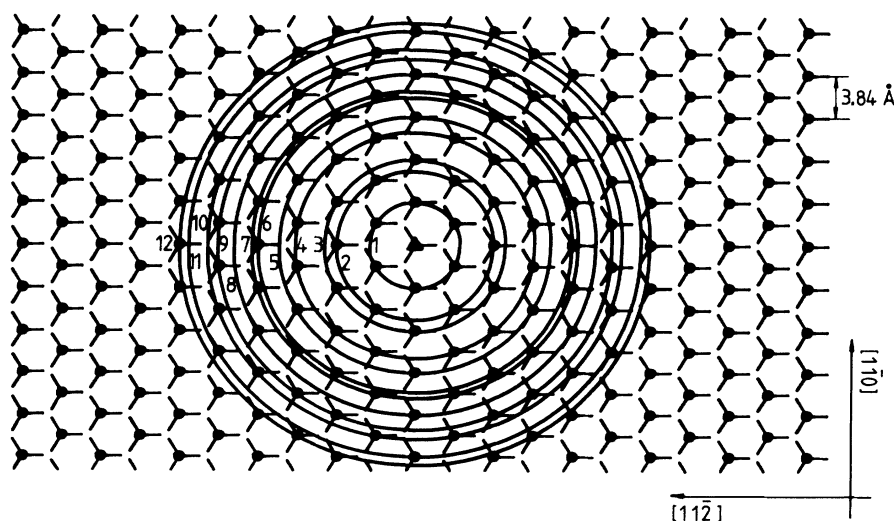


FIG. 7. Schematic top view of an unreconstructed (111)Si surface. The lines, pointing out of each Si atom (●), represent the Si—Si bonds with the underlying atoms of the crystalline silicon. The interatomic distance at the interface is $a_L = 3.8426$ Å, rendering a surface Si atom density of $N_a = 7.830 \times 10^{14}$ cm⁻². The circles identify the first- through twelfth-nearest-neighbor shells with respect to the central Si atom (▲).

count for the unresolved hyperfine broadening.

An important item in practical calculations is the size of the circular region sampled, that is, the number of allowed Si sites N_{al} and spins n enclosed. Finite computation time and computer memory limit n to $n_{max}=12$ and, accordingly, N is limited to $N_{max} \approx n_{max}/f$ (or, equivalently, N_{al} is limited to $N_{al,max} \approx n_{max}/f'$). Indeed, the rank of the Hamiltonian matrix increases exponentially with the number of interacting spins n (for n spins the rank is 2^n) and the number of operations for solving the eigensystem jumps up as the cube of the rank. The impact of the n_{max} restriction is best illustrated by plotting the relative absorption peak heights of the n -spin dipolar histograms for the random-distribution model and $N=1573$ (i.e., an improved extension of Fig. 9 of Ref. 24). This shows that, for $f=2 \times 10^{-3}$, dipolar histograms up to $n=8$ —thus $n_{max} \geq 8$ —are needed for a reliable representation of the total histogram, while with $n_{max}=12$ and $N=1573$, reliable dipolar spectra can only be calculated for $f \lesssim 5 \times 10^{-3}$. This is a main limit of the present calculations.

Hand in hand with the n_{max} limitation goes the requirement that the circular (111)Si surface region sampled has to be large enough so as to avoid the situation where the calculated dipolar spectra depend on the chosen region size d , which would lead to an intolerable calculation artifact. This imposes an underbound N_{min} for N . The impact of this has been evaluated within the random distribution model by its effect on the calculated ΔB_{pp} using the calculated residual line shape $R2$ (Sec. IV B) of width $\Delta B_{pp}^R = 1.29$ G. The total (DD and hyperfine) linewidth ΔB_{pp} was calculated for $f=5 \times 10^{-3}$ for three values of N , as plotted in Fig. 8; the $N=1$ value,

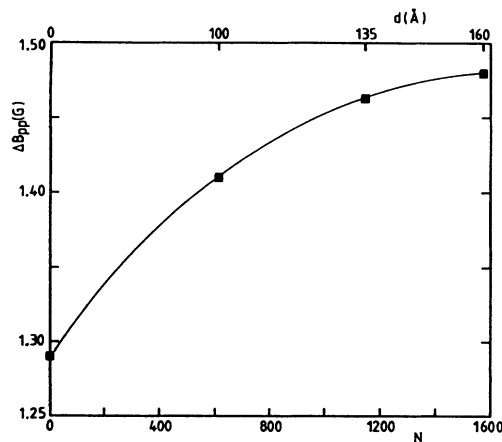


FIG. 8. Dependence of the calculated dipolar ESR broadening for P_b centers at the (111)Si/SiO₂ interface on the size of the circular sampling region (enclosing N Si atom sites, all allowed as possible P_b sites) in an unreconstructed (111)Si plane. Calculations are carried out for $f=5 \times 10^{-3}$ and $\mathbf{B} \parallel [111]$ using residual curve $R2$ (see Fig. 6) as convoluting broadening shape. The curve represents a polynomial fit. Though the absolute differences may appear small, there is still a significant relative increase in the dipolar width in going from an $N \approx 600$ to an $N \approx 1600$ region. Note that the curve has nearly reached its plateau for $N=1573$.

of course, is the residual (zero DD broadening) linewidth. The absolute changes in ΔB_{pp} are small. Indeed, ΔB_{pp} increases from 1.41 G for $N=613$ to 1.48 G for $N=1573$, which is an increase of only 0.07 G. However, when we compare the changes in dipolar broadening, the difference is significant. Starting from $\Delta B_{pp}^R = 1.29$ G, the dipolar broadening reaches 0.12 G for $N=613$ to increase to 0.19 G for $N=1573$ —still an increase of 58% in going from $N=613$ to 1573. It is evident that underestimating N will lead to intolerable errors in ΔB_{pp} at higher f . Clearly, though, the dependence of ΔB_{pp} on N for $f=5 \times 10^{-3}$ starts to flatten out for $N \rightarrow 1573$. We thus conclude that $N_{min} \geq 1573$ is required for $f=5 \times 10^{-3}$ and that reliable calculations can be carried out for f up to $\approx 5 \times 10^{-3}$. As will be explained in Sec. V C, this is a significant improvement of previous calculations²⁴ covering only 613 sites with $n_{max}=6$. We will henceforth use $N=1573$ in all our further calculations where experiment and theory are directly compared. A (111)Si surface region comprising $N=613$ Si atoms, though, will be used to compare theoretical spectra calculated for different networks of allowed P_b sites. Although the linewidths are underestimated, it is still possible to compare the line shapes and the f dependence of the spectra.

Dipolar spectra were calculated for five different models (arrays) of allowed sites, of which the calculation procedure will be outlined briefly. The physical relevance of the models will be discussed in the next section. These arrays were selected as a representative cross section of all plausible P_b distributions one could expect, based upon the present microscopical understanding of the Si/SiO₂ interface.

Model 1 is a calculation for the most general array, i.e., all Si atoms at the (111)Si/SiO₂ interface are allowed to be the site of a P_b defect, over which the P_b centers are randomly distributed (the random-distribution model). The calculation of the dipolar spectra for this model has been explained above. The n -spin dipolar histograms are shown in Fig. 9 for $n=1-12$ and $N=1573$. They were calculated as an average over all possible spatial P_b configurations for $n=2$, over 100 000 configurations for $n=3-8$, and over 10 000, 2000, 400, and 100 configurations for $n=9, 10, 11$, and 12, respectively. Comparison of the histograms of Fig. 9 with Fig. 4 shows the positions of all resolved fine structures to be identical, giving confidence to the local-field approximation.

In model 2, the only possible sites of P_b defects are assumed to be Si atoms aligned along a certain crystal axis in the (111) plane. Such a model would comply with the suggestion that P_b defects prevail at interfacial ledges. The array considered for a particular axis is the linear chain of Si atom sites with Si-Si site spacing as occurring along the corresponding c -Si axes. The number of chains per cm² of interface is chosen in agreement with the typical density of ledges (terrace borders) as observed experimentally.^{2-4,59} The value for N_{min} can now be taken much lower ($N_{min} \approx 40$). The spin distribution on this one-dimensional Si array is supposed to be random, so that the formulas of model 1 also apply to this case. However, when comparing theory with experiment, it must be realized that the fractional site occupancy f' on

the 1D lattice relates to the experimentally obtained fractional occupancy f as $f' = fN/N_{\text{al}}$, where $N_{\text{al}}/N \ll 1$ is the fraction of the (111)Si surface atoms at the 1D array. Model-2 calculations were carried out for P_b arrays along the $[\bar{1}\bar{1}0]$ and $[\bar{1}\bar{1}\bar{2}]$ crystal axes.

The array of possible P_b sites in model 3 is determined by looking at the (111)Si surface as consisting of a structure of hexagonal Si rings; the array considered is then formed by the Si atoms at the center of those hexagonal rings, which form a 2D net of the same crystal symmetry but with a different orientation and lattice constant, i.e., $a_L = 10.167 \text{ \AA} = \sqrt{7} \times 3.8426 \text{ \AA}$, where 3.8426 \AA is the lattice constant of the general (111)Si net. A schematic

diagram of this array (large dots) is shown in Fig. 10. Each of them is surrounded by six Si surface atoms, connected to each other by a dashed hexagon. It is easy to see that the symmetry of the "heavy" net is identical to the symmetry of the unreconstructed (111)Si surface. So the calculations are identical to model 1 except for the different lattice constant and a computational fractional site occupancy f' , which is seven times larger than the experimental value f . The physical reasons for considering such a rescaled net will be evidenced below.

Models 4 and 5 consist of modifications of model 1 resulting from introducing correlations in the "random" distribution of P_b 's over the allowed sites. The P_b defects

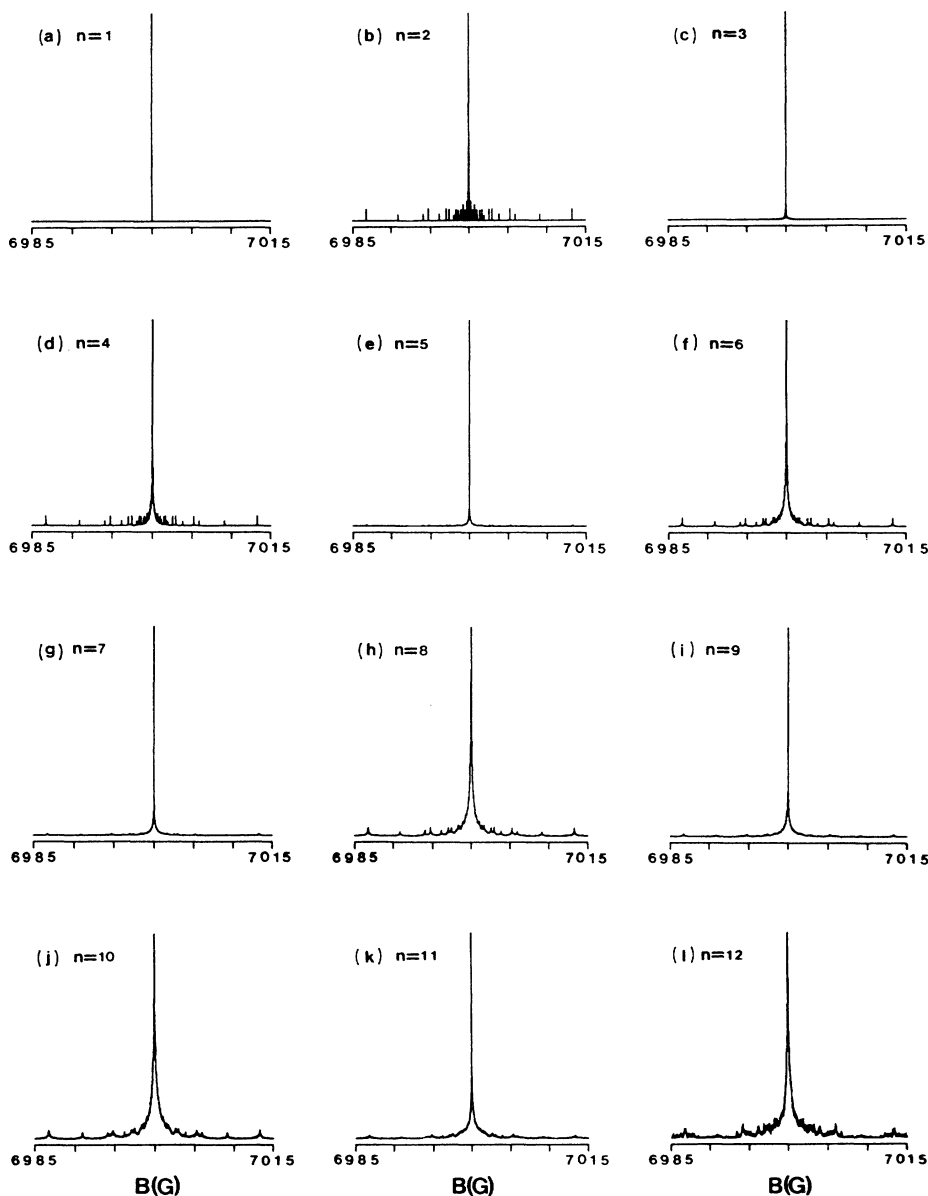


FIG. 9. Dipolar histograms for $n=1-12$ interacting P_b spins ($S=\frac{1}{2}$) in the random-distribution model. The calculations were carried out on a circular unreconstructed (111)Si surface containing $N=1573$ Si atoms and $\mathbf{B}||[111]$. The $n=1$ dipolar histogram (a) represents the Zeeman resonance. The $n=12$ histogram, which is an average over 100 configurations of P_b defects on the (111)Si region, represents the highest number of interacting P_b spins that could still be calculated with the present calculation capacity.

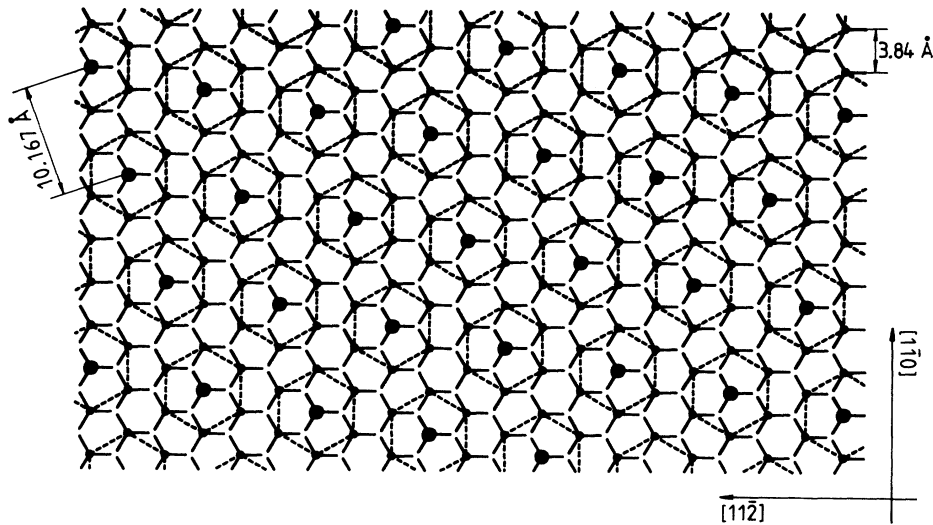


FIG. 10. Schematic top view of the net of allowed P_b sites (large dots) in interface model 3, constructed on a view of a $(111)\text{Si}$ surface (Fig. 7). Each Si atom of the net is surrounded by six Si atoms (not belonging to the net), connected by a dashed hexagon. The model-3 net exhibits the same symmetry as the $(111)\text{Si}$ surface but with a different lattice constant $a_L = 10.167 \text{ \AA} = \sqrt{7} \times 3.8426 \text{ \AA}$, and a seven times lower atom density.

are made to cluster in model 4, whereas in model 5 the separation between the P_b defects tends to be enhanced (clustering avoided). The distribution function is calculated by assigning each Si atom in the (111) plane a different probability of being the site of a P_b defect, depending on the configuration of the P_b defects already allocated. The latter information is used to stochastically select the next P_b site. Different distribution functions were tried for the calculation of the site probability, but all gave more or less identical results at the low f encountered. The region over which the spins are distributed was chosen much larger than in the previous models; the DD calculations, however, were carried out on a subregion of the surface containing $N = 1573$ Si atoms. Because of the deviation from the random-distribution function, the linear combination coefficients of the various n -spin dipolar histograms in Eq. (21) were determined statistically this time, instead of being given by the binomial distribution.²⁴

V. COMPARISON OF THEORY WITH EXPERIMENT

In Sec. III, the P_b linewidth variations were conclusively identified as resulting from DD interaction using mainly qualitative arguments. The purpose of this section is to present a quantitative comparison between experiment and calculations for both the linewidth-versus- f dependence and resonance line shape. It is hoped in this way to obtain information on the in-plane distribution of P_b defects.

A. Low- f spectra ($f \lesssim 5 \times 10^{-3}$)

The devising of site arrays for which DD calculations are carried out, that is, the search for the array of possible Si atom sites at the $(111)\text{Si}/\text{SiO}_2$ interface plane over which the P_b centers are distributed, is best guided by the

present knowledge of the interface structure. Fortunately, various microscopic methods have recently provided detailed information, which is pictured in Fig. 11. Using HRTEM,^{2,4,24} x-ray photoelectron spectroscopy (XPS),⁶⁰ and low-energy electron diffraction (LEED),^{3,59} the $(111)\text{Si}/\text{SiO}_2$ interface has been shown to be atomically abrupt, consisting of atomically flat terraces separated by ledges, typically 1–3 atoms high and 110–220 \AA apart. This corresponds to step atom densities N_{step} in the range $(3.3\text{--}6.6) \times 10^{13} \text{ cm}^{-2}$. According to one report,³ the otherwise perfect terraces comprise small domains of inhomogeneities (patches), three to eight atomic distances wide on average. But in contrast with the terrace and ledge structures, these are strongly dependent on the applied post-oxidation annealing. While there is general agreement on the abruptness of the interface, the nature of the structural matching of the SiO_2 to the $(111)\text{Si}$ surface is still controversial. Many earlier works reported that the interfacial oxide is amorphous and Si-rich, but this description is fundamentally questioned by recent observations. By growing thermal oxides on silicon, prepared by the molecular-beam-epitaxy (MBE) method, Ourmazd, Rentschler, and Bevk⁴ concluded from HRTEM observations that the interfacial oxide is, in fact, crystalline over about 7 \AA deep into the oxide, the crystalline phase closely resembling tridymite. This may be compared with a previous conclusion⁶¹ indicating that the short-range order in SiO_2 as obtained by x-ray and neutron-diffraction experiments, most closely relates to the tridymite structure. When carrying out calculations on the P_b center at the $(111)\text{Si}/\text{SiO}_2$ interface, Cook and White¹³ found that the interfacial SiO_2 layers could most easily be modeled by tridymitelike puckered ditrigonal rings of six SiO_4 tetrahedra, as these could be matched to the underlying $(111)\text{Si}$ surface without great distortions of

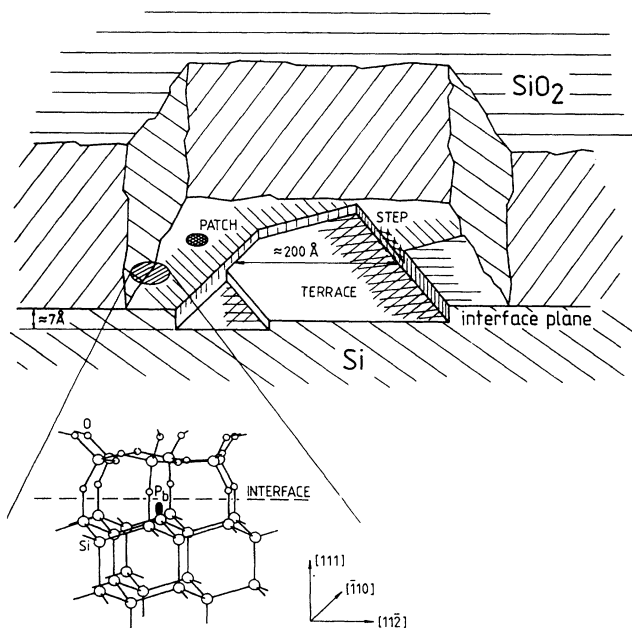


FIG. 11. Schematic picture of the present microscopical understanding of the (111)Si/SiO₂ interface structure, showing the characteristic features, i.e., terraces, ledges, and patches. The enlarged view shows a ball-and-stick model of the P_b cluster as proposed in Ref. 13; the immediate silica cap of the unpaired P_b bond is formed by a puckerd, ditrigonal ring of six SiO₄ tetrahedra (the *c*-tridymitelike model).

the bond angles or interatomic distances (see enlarged view in Fig. 11). We will refer to this as the *ditrigonal ring* or *tridymitelike* model. The atomic abruptness of the (111)Si/SiO₂ interface indicates that the P_b interface defects are essentially distributed over one (111)Si interface plane, as concluded before.¹ This is a basic assumption underlying all further theoretical models.

The key question, then, is where the P_b defects fit into this interface picture. With what particular interface structure(s) are they connected? Are they created during cooling off of the interface after oxidation, or rather, are they created solely as a result of the natural Si/SiO₂ mismatch during the oxide growth? In the latter case, the P_b defects are perhaps essential in establishing the particular interface structure. If so, the interface structure and the P_b defect distribution will be correlated. If the P_b defects would, indeed, coestablish the interface structure during oxidation, e.g., by release of interfacial strain, then they should be generated in reproducing quantities leading to a more or less universal interface structure, as observed. From the combined understanding of P_b distribution and interface structure, that is, disclosure of the array of possible P_b sites, we could then stand a fair chance of understanding the physical mechanism(s) by which they are formed. In this way the present dipolar calculations might also lead to information on the interface structure. Obviously, within the experimental evidence just summarized, there are three main interface features, i.e., ledges, terraces, and inhomogeneity patches, to which the P_b centers may be linked.

A first possibility is that P_b defects might only reside at steps, which, depending on one's view, may be seen as preferred dangling-bond locations. This is represented by model 2, referred to as the step model. If this model would apply, it is probably the easier one to test. Indeed, in contrast with the other models, the configuration of the spins is one dimensional in this case, so that unique ESR properties, such as a highly anisotropic linewidth and line shape,⁶² may be expected.

A second possibility is that the P_b centers may be part of the inhomogeneity patches, which is represented by model 4. This is very unlikely, as the concentration of inhomogeneity patches is strongly dependent on the oxidation conditions and post-oxidation annealings,³ whereas (in the absence of H) the P_b defects seem to be unaffected.³³ However, if this case would apply, the dipolar line shape would certainly resemble that of a strongly clustered P_b distribution, which will be discussed below.

Third, the P_b defects may only reside at terraces. Yet in this case there remain many different ways to incorporate them, and several arrays of possible P_b sites, each devised to meet a certain physical insight, may be envisaged. First, if assuming that the defects are created as a result of random strain release, then one might expect a random distribution of P_b centers over all Si atom sites in a (111) plane; this is the model-1 situation (the random-distribution model). But if efficient strain relaxation would only occur by interface adaptation over finite regions, P_b defects could show a tendency to cluster. This, in fact, leads to the same conclusion as the above (patches) model 4. As a second alternative, it may be presumed that the strain release by generating a P_b at a certain site may be sufficient so that the critical stress limit for a P_b generation is not reached anymore in the immediate neighborhood. The P_b defects will then tend to be separated further apart than a random distribution would imply—i.e., “self-avoiding will tend to be”—which is the basis of model 5. The suggestion²⁴ that P_b defects are generated as a result of the release of strain energy from finite regions of the interface during the cool-down period after thermal oxidation leads to a similar conclusion. Third, regular arrays could be imagined if we suppose that the P_b centers somehow coestablish the particular interface structure. One such array may be inferred from the tridymitelike model, leading to model 3 (see Fig. 10). This model is of particular interest because there appears to be some experimental evidence⁴ for it from HRTEM observations. It also suggests an interesting explanation for the fact that the P_b defects may readily be reversibly passivated by the H radical, and not by other chemical species.¹³ The size of the opening (≈ 1.4 Å) of the capping ditrigonal silica ring (cf. Fig. 11) would be such as to permit the H radical to reach the unpaired bond, but would protect the P_b unpaired bond from passivation by large radical species present in the SiO₂ layer. In the case where the interface transition is crystalline, the six-membered rings will cover the Si surface in a close-packed way, and the central Si atoms, which are possible dangling-bond sites, again make up a 2D triangular net of lattice constant $\sqrt{7}$ times larger than that

of the most general net; this is the physics behind model 3. If the six-membered rings are not close packed, the model essentially reduces to a variant of model 1.

P_b ESR spectra calculated for $f=5 \times 10^{-3}$ for all models are depicted in Fig. 12 for the five models (arrays) considered. Residual line shape $R2$ (including the shf peaks; see Fig. 6) is used in the convolution of the dipolar histograms. The respective linewidth and κ variations versus f are plotted in Fig. 13. All spectra contain the same qualitative features characterizing the experimental line shape, i.e., a central line (A), a partially resolved fine-structure doublet (B), observed as "shoulders" on the central line, and some additional (partially) resolved doublets. The central line A and the strong doublet B are easily recognized in the experimental spectra (see Fig. 3); the identification of the other weaker doublets seems more problematic due to overlapping structure. Based on calculations for $N=613$ (111)Si regions, the gross features of the different spectra (models) are compared with experiments in order to select the most likely model. The final model will then be analyzed in detail from $N=1573$ calculations.

The calculated dipolar spectra in Fig. 12 can be divided into three groups along the P_b concentration dependence of ESR parameters. The first group consists of models 1 (random distribution), 3 (ditrigrinal ring), and 5 (self-avoiding), which exhibit a similar f dependence of all three parameters ΔB , ΔB_{pp} , and κ , as shown in Fig.

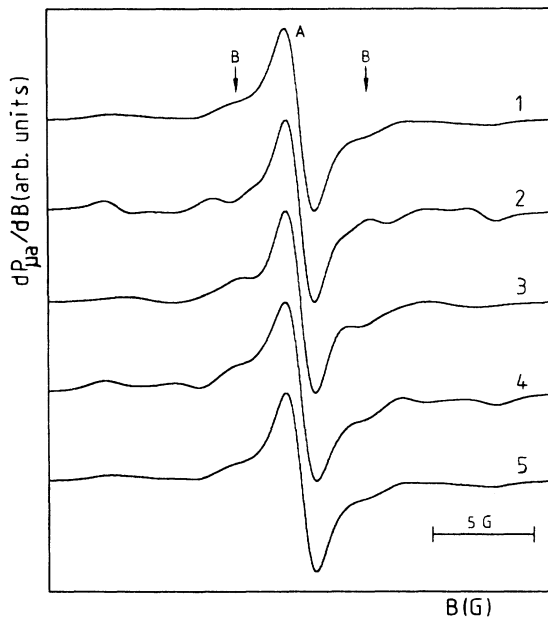


FIG. 12. Theoretical P_b spectra for $f=5 \times 10^{-3}$, $\mathbf{B} \parallel [111]$, and $N=613$ for five different arrays of Si-atom sites at a (111)Si/SiO₂ interface over which the P_b 's are randomly distributed: (a) most general net, comprising all Si atom sites in a (111) plane, (b) array of surface steps oriented along $[1\bar{1}0]$, (c) 2D triangular net of $a_L=10.167$ Å, modeled for a c-tridymite (SiO₂)/Si transition, (d) clustered P_b distribution over the same array as (a), and (e) "self-avoiding" distribution of P_b 's over the same array as in (a).

13. This, in fact, should not come as a surprise, particularly in light of the low- f values considered. All three underlying models are 2D arrays of Si sites, over which the P_b centers are *dilutely* and *randomly* distributed (in model 5 the spins have a tendency to avoid each other, but because of the low f considered, the influence of this is minimal). There are, however, distinct spectral differences. The fact that the spins in model 3 are distributed on an array with a different lattice constant has a profound influence on the dipolar spectrum. As compared with spectra 1 and 5 (Fig. 12), spectrum 3 exhibits a well-resolved, strong B doublet,⁶³ unlike experimental observations (cf. Fig. 3) for $f=5 \times 10^{-3}$. This eliminates model 3. Spectra 1 and 5 are, however, closer to experimental observations.

The second group is formed by model 2, the step model. The fractional site occupancy f' for the array composed by the linear chains (steps) is calculated as $f'=f(N_a/N_{\text{step}})=7.9 \times 10^{-2}$, where^{3,59} $N_{\text{step}} \approx 5 \times 10^{13}$ cm⁻². In comparison to the other curves shown in Fig. 12, spectrum 2 exhibits markedly more resolved fine structure and a smaller linewidth (both ΔB and ΔB_{pp}). The latter is also reflected in the linewidth-versus- f dependence (see Fig. 13), which shows a distinctly smaller

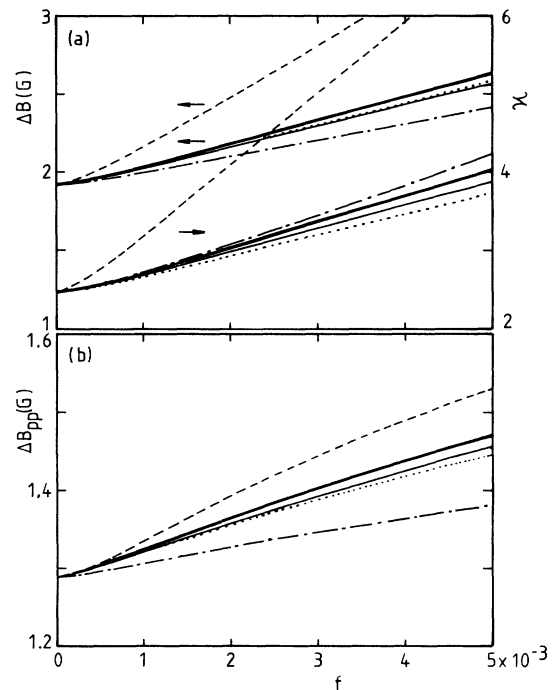


FIG. 13. Theoretical dependence of absorption linewidth ΔB and line-shape factor κ [in (a)], and peak-to-peak width ΔB_{pp} on f for $\mathbf{B} \parallel [111]$ of the P_b resonance calculated for five different models, i.e., arrays of possible P_b sites in a (111)Si plane. Calculations were carried out for a (111)Si/SiO₂ region encircling $N=613$ Si atoms. Model 1, random P_b distribution model (solid curves); model 2, random P_b distribution along a $[1\bar{1}0]$ step axis (dash-dotted curves); model 3, ditrigrinal ring model supposing a tridymite (SiO₂)/Si-like transition (dotted curves); model 4, clustered P_b distribution (dashed curves); model 5, "self-avoiding" P_b distribution (bold solid curves).

increase of linewidth ($\Delta B_{pp} = 1.38$ G at $f = 5 \times 10^{-3}$) with increasing f . Comparison with the experimental signal shape in Fig. 3 clearly rejects the step model, though the behavior of κ is similar to the models of group 1. This is well understood from the local-field calculations,⁴¹ which indicate that with decreasing dimensionality, the resolved dipolar fine structure will enhance due to the less-effective averaging. As this resolved fine structure contributes little to the width of the central line, the weaker broadening with increasing f follows naturally.

The disagreement of the step model with experiment affirms other experimental facts.²³ In conventional (111)Si/SiO₂, only the P_b defects with the unpaired orbital perpendicular to the interface are observed, which exhibit a sharp resonance. No P_b defects with unpaired sp^3 orbitals along "equivalent" directions ($[\bar{1}11]$, $[1\bar{1}1]$, or $[11\bar{1}]$) are observed,¹⁸ which means that surface irregularities, such as steps, are no essential part of the immediate P_b structure. Depending on one's opinion, this may not come as a surprise. If strain is to be released at the interface, the irregularity formed by a step may be a natural means of lattice adaptation, such that there might be no need for the matching lattices to generate additional unpaired Si bonds there.

The last group is made up by model 4, the cluster model. Similar to the step model 2, spectrum 4 (see Fig. 12) shows much-resolved fine structure and a strong B doublet, unlike experimental observation. The increase of all three line-shape parameters with f shown in Fig. 13 is much stronger than for the other models. In particular, the f dependence of κ deviates profoundly from what is observed experimentally (Fig. 2), thus clearly negating the cluster model.

The above comparison leaves as the most probable model a P_b defect interface distribution in which the P_b centers are randomly distributed at the interface terraces—the so-called random distribution model (model 1). For low f , model 5 essentially reduces to the random-distribution model, so that a clear distinction between the two models appears as of yet unfeasible. Probably, this must await correct simulation of high- f ($\geq 1\%$) ESR spectra.

The final step then is to compare this random-distribution model in quantitative detail with experimental observations to check for the model's adequacy. It has been demonstrated before that a $N = 613$ (111)Si sampling region used above is too small to render correct quantitative data. Instead, $N \geq 1573$ was required for $f \leq 5 \times 10^{-3}$, leading to the calculation of the n -spin dipolar histograms ($n = 1-12$) for the random-distribution model on a (111)Si/SiO₂ surface region containing $N = N_{al} = 1573$ Si atoms, as shown in Fig. 9. With these the total dipolar histogram for $f = 4 \times 10^{-3}$ was constructed, and theoretical P_b resonances were calculated by convoluting with each of the three residual line shapes presented in Sec. IV B. The results are shown in Fig. 14. The dependence of ΔB , ΔB_{pp} and κ on f was calculated for each residual line-shape model and is illustrated in Fig. 2.

It needs to be mentioned that the "theoretical" P_b concentrations (i.e., f 's) used to calculate spectra were taken

slightly larger than the experimental one as a result of two corrections. As mentioned earlier, a first one (of about 4.9%) stems from not having included the main ²⁹Si hf ($A_{||} \approx 156$ G) doublet in the integration of experimental spectra to determine $[P_b](f)$. The second correction, likely resulting from antiferromagnetic spin pairing, will be treated further on.

The quantitative agreement between theory and experiment revealed in Fig. 2 is quite satisfactory for all three residual profiles. This is particularly true if one realizes that it concerns the comparison of absolute measurements and *ab initio* theoretical calculations. The fit of all three ΔB_{pp} -versus- f curves to the data is nearly equally satisfactory; the scatter between these curves is minor, making them an excellent criterion to distinguish be-

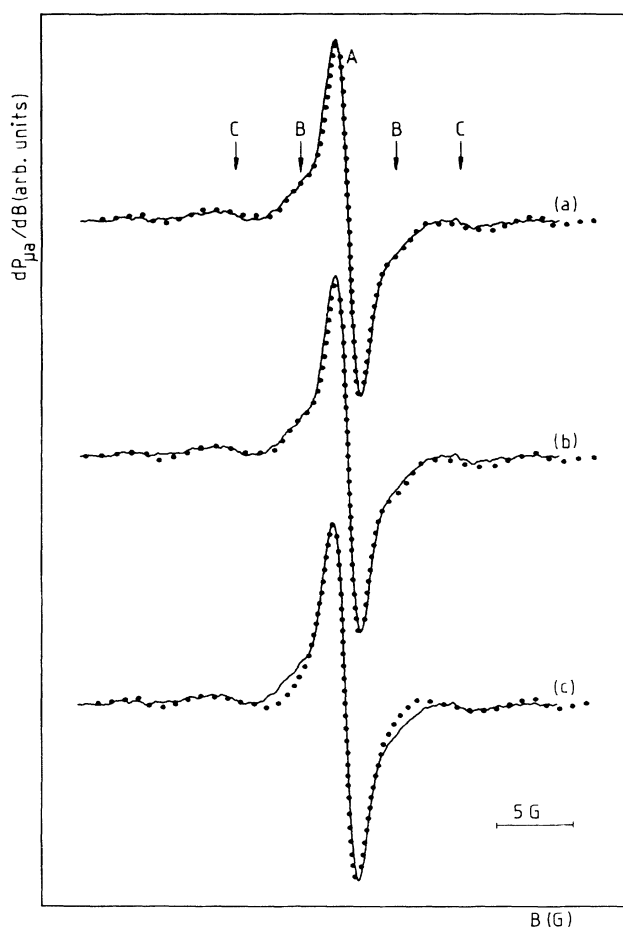


FIG. 14. Fitting of theoretical dipolar spectra to the experimental 20.2-GHz P_b signal for $f = 4 \times 10^{-3}$ and $\mathbf{B} \parallel [111]$ measured at 4.3 K. The theoretical curves were obtained by calculating the dipolar histogram for a random-spin distribution ($S = \frac{1}{2}$) on a (111)Si/SiO₂ region encircling $N = 1573$ Si atoms (random-distribution model) which was subsequently convoluted with (see Fig. 6) (a) residual spectrum $R1$: sum of Gaussian profiles; (b) residual spectrum $R2$: parametrized hf cluster calculation; (c) residual spectrum $R3$: based upon a Si₂₂H₂₇ P_b cluster hf calculation [see Ref. (13)]. The ²⁹Si shf doublet of $A_{||}^{shf} = 14.8$ G (see Fig. 15) has been included.

tween the different P_b distribution models. The theoretical ΔB -versus- f and κ -versus- f curves, however, show a larger spread between the various residual broadening shapes, thus allowing for a more in-depth test of the random-distribution model as regards the most adequate residual broadening function. The residual model-R2 curves show the best overall agreement with the experimental data and a nearly perfect trend towards higher f , for which, as explained, no calculations could be carried out because of practical constraints.

A crucial test of the residual broadening function in combination with the random-distribution model is pictured in Fig. 14, showing an experimental spectrum ($f=4 \times 10^{-3}$) together with three theoretical line shapes, each calculated by means of one of the residual line shapes. The *A*, *B*, and *C* structures, which have been observed experimentally (see Fig. 3), are also indicated. The fittings of the central line (signal *A*) and structure *C* appear satisfactory for all three models. The intensity of doublet *B*, however, is clearly underestimated in spectrum (c), whereas it is perfect for the other two cases (a) and (b). This may seem somewhat surprising, as all three spectra in Fig. 14 are calculated from the same dipolar histogram, and none of the residual profiles in Fig. 6 exhibits shoulders with an intensity close to the *B*-doublet intensity. Yet, the *B*-doublet intensity appears significantly "tunable" by just changing the shape and the extension of the residual profile's shoulders, which affects the ΔB -versus- f and κ -versus- f curves as well. This just bears out the sensitivity of the ultimate dipolar signal shape to the details of the residual ($f \rightarrow 0$) broadening spectrum, which lends some support as regards the selection of the correct theoretical residual shape. At first glance, the overall fitting quality of the curves (a) and (b) pictured in Fig. 14 seems equally successful. Yet, in agreement with the conclusions from Fig. 2, it follows from overall line-shape fittings over many experimental observations and taking into account all details, which are somewhat difficult to demonstrate in the singular fit pictured in Fig. 14, that the residual line-shape model R2 is most adequate.

There is one further remark regarding the residual spectra R2 and R3. As mentioned, these have been calculated using identical equations [Eqs. (12)–(16)] but with different hf splitting parameters $A_{\parallel i}$. Residual spectrum R3 was obtained from an elaborate *ab initio* Si₂₂H₂₇ P_b cluster calculation,¹³ while R2 is just an adjusted version of this. It would follow from the less-than-ideal fit (c) in Fig. 14 and a comparison of the respective $A_{\parallel i}$ values of the models R2 and R3 tabulated in Table I that the parameters of R3 are underestimated. This, however, is not kept as proof that the $A_{\parallel i}$ parameters of residual model R2 are unique in any way—the number of adjustable parameters is large. They were just obtained as one possible set of parameters leading to a correct fitting of experimental results. Instead, the main result of this analysis is that it disfavors some theoretical residual line shapes.

Summarizing, a first conclusion is that the hf parameters $A_{\parallel i}$, calculated for the particular Si₂₂H₂₇ P_b cluster,¹³ are too small to obtain satisfactory agreement with experimental spectra at higher f . This may be due either to

the use of Fermi-contact hf parameters instead of the full (isotropic plus anisotropic) hyperfine parameters or, more fundamentally, to a theoretical underestimation of the full hyperfine parameters themselves. Second, the analyses of both the low- and high- f spectra suggest residual spectrum R2 as the best representation of the P_b line shape for $f \rightarrow 0$.

We now proceed to a more-detailed analysis of the structure revealed in the experimental P_b spectra. A step-by-step buildup of the calculated spectrum (b) in Fig. 14 is shown in Fig. 15. Spectrum S1 represents the theoretical P_b dipolar line shape for $f=4 \times 10^{-3}$, calculated with residual profile R2 (see Fig. 6) in the absence

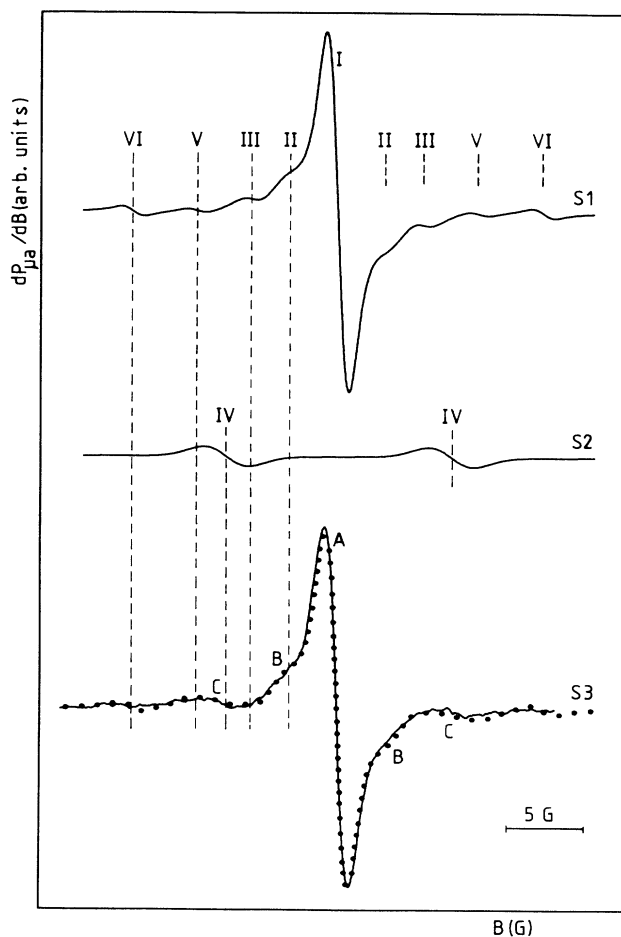


FIG. 15. Detailed buildup of theoretical P_b spectrum (b) of Fig. 14, exposing the fine structure and shf features. The calculations are carried out for $\mathbf{B} \parallel [111]$ and $f=4 \times 10^{-3}$ within the random-distribution model using residual profile R2 (see Fig. 6) as convoluting broadening function. S1: theoretical P_b resonance line shape in the absence of the ^{29}Si shf doublet. Signal I represents the P_b Zeeman resonance. The fine-structure signals, labeled by roman numbers, are due to fourth- (VI), fifth- (V), sixth- and seventh- (III), and eighth-, ninth-, and higher-order (II) nearest-neighbor dipolar interactions. S2: ^{29}Si shf doublet (labeled IV) for $\mathbf{B} \parallel [111]$ ($A_{\parallel i}^{\text{shf}}=14.8$ G). S3: sum of the theoretical profiles S1 and S2 (dots) superposed on an experimental P_b resonance (solid line) observed at 4.3 K. The structures, which are clearly observed experimentally at $f=4 \times 10^{-3}$, are labeled A, B, and C.

of the ^{29}Si shf doublet. The characteristic structural features are labeled by roman numbers. Signal I represents the central line in the absence of all dipolar and hf interactions. The origin of the fine structure can be identified from comparison with the fine structure of the n -spin dipolar histograms pictured in Fig. 9 or by comparison with the histogram in Fig. 4—a result of the local-field approximation. In this way we find that the fine-structure signals VI and V originate from dipolar interactions between fourth and fifth nearest neighbors, respectively. The sixth- and seventh-nearest-neighbor interactions make up fine-structure signal III, whereas signal II is the added result of eighth-, ninth-, and higher-nearest-neighbor interaction. Spectrum S_2 represents the ^{29}Si shf spectrum resulting from hf interaction of the unpaired P_b electron with the three nearest-neighbor Si nuclei in the bulk as used in the present simulation, with $A_{\parallel}^{\text{shf}} = 14.8 \pm 0.2$ G and total intensity of 14.7% of spectrum S_1 . This doublet is labeled by roman number IV. The sum of spectra S_1 and S_2 is shown by dots in S_3 , whereas the solid line in S_3 represents the same experimental spectrum as shown in Fig. 14 ($f = 4 \times 10^{-3}$). Comparison of S_1 and S_3 immediately identifies the theoretical signal I as the experimental line A and the dipolar fine structure II as the shoulders B . Fine-structure signal VI, however, is *not* observed experimentally.

The structure C , which was previously ascribed^{10–13} to the ^{29}Si shf doublet, is in fact a superposition of several signals, that is, the theoretical ^{29}Si shf doublet IV and the fine-structure doublets III and V. The latter are nearly symmetric relative to the shf doublet IV so that, when added together, the signals III, V, and IV result in the smoothed and broadened signal C as compared to signal IV. The perfect fit of the experimental C region obtained by adding the calculated spectra S_1 and S_2 conclusively demonstrates the presence of the shf doublet, and allows unequivocal determination of the shf splitting and signal strength. The assignment of the shf doublet, which was predicted on theoretical grounds^{11–13} in P_b experimental spectra, has so far necessarily been speculative, as the dipolar and shf structures have not been separated. When the S/N ratio is not very high, part of the blurred shf signal intensity may be lost during the double numerical integration of the derivative spectrum. Unless the DD-interaction effects have been well separated, this will make it extremely difficult to draw any conclusion⁴⁶ from the experimentally determined intensity of C relative to A and B regarding the nature (i.e., the number of interacting equivalent neighboring nuclei) of the shf signal. Moreover, it explains why at higher f the structure C seems to “split up” in more signals (see Figs. 3 and 16); in particular, doublet D becomes well resolved. Indeed, whereas the intensity of the shf doublet remains relatively unaltered with rising f , the dipolar fine-structure doublets III and V *do* grow relative to signal A . This causes structure C to blur, and, eventually, to split up in the two fine-structure signals III and V, and shf signal IV at higher f . This overshadowing of the shf structure by fine structure demonstrates that assigning the shf doublet at high f ($\geq 1\%$) requires extreme care.

It was mentioned in Sec. III that scrutinizing experi-

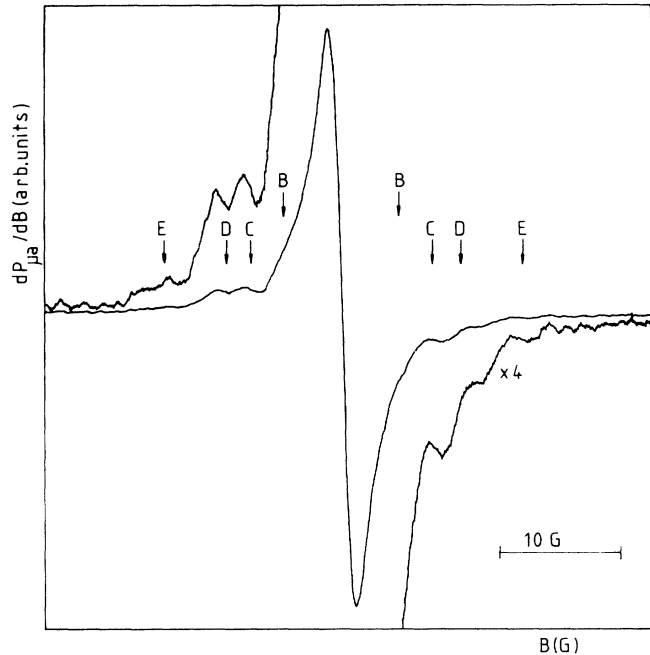


FIG. 16. High-concentration ($f = 0.016 \pm 0.001$) P_b signal observed on (111)Si/SiO₂ at 4.3 K and 20.2 GHz with $P_{\mu} < -63$ dBm for $\mathbf{B} \parallel [111]$. A rich structure is clearly observed around region C . The doublets C and D are ascribed to ^{29}Si shf structure and fifth-neighbor pair DD interaction (fine structure), respectively. The signals E , of splitting ≈ 27 G, though competing with the noise, are likely remnants of the fourth-neighbor pair DD interaction.

ments were carried out to search for eventual fine-structure signals with larger field splittings (i.e., ≥ 20 G)—without any success, however. In a first explanation, the absence of fine-structure signals due to first-, second-, third-, and fourth-nearest-neighbor interactions could be ascribed to too low an S/N ratio. It is believed, though, that these fine-structure signals should have been observable with the present S/N ratio realized if they would have occurred with relative intensities as predicted by theory, e.g., as depicted in Fig. 15 (doublet VI on curve S_1). A second reason may be the total absence of, or at least a very much reduced, probability of the occurrence for first, second, third, and fourth nearest neighbors due to the particular Si site array of allowed P_b sites in the (111)Si plane, e.g., in the sense of the self-avoiding array of model 5. Indeed, first, second, third, and fourth neighbors do not occur in this model for $f \lesssim 3\%$. As mentioned, the previous low- f calculations were not able to rule out model 5 as a possible alternative for the random-distribution model. A third, more-favored explanation is the presence of superexchange interactions between nearby (rendering large DD splittings) P_b spins. These may induce an antiferromagnetic coupling of the spins and, consequently, the disappearance of the ESR signal. This interaction has not been included in our spin Hamiltonian up to now, and may therefore be a natural explanation for the unobserved fine structure. This interpretation, however, requires a justification of the magnitude (strength) J'' of the superexchange coupling

coefficient.

It has been pointed out before that an accurate estimate of the superexchange interaction range and strength is hard to achieve. But, instead, we can compare the P_b results to experimental data on superexchange between spins in dangling-bond-like orbitals in bulk silicon. Although the presence of exchange between $S=1$ deep-level defects in bulk silicon is well established, accurate values for the interaction coefficients are seldom obtained; the majority of these defects can only be observed at $T=4.2$ K using light excitation to populate the paramagnetic spin-triplet levels.^{64,65} Lee and Corbett⁵⁷ could deduce a value for the isotropic superexchange constant J'' between two spins a distance $r_{SS}=6.72-7.68$ Å apart from a comparison of the g and D tensors of double and triple vacancies containing a different number of oxygen atoms. They found that $J'' \sim 0.01$ eV. As the P_b defect electrons at the (111)Si/SiO₂ interface are situated in prototype dangling-bond orbitals in a silicon and oxygen environment, we may argue that the superexchange interaction coefficient J'' between the third-neighbor dangling bonds

($r_{SS}=7.68$ Å) should be of the same order of magnitude. In analyzing resolved fine structure on calculated P_b spectra, it should be noted that the intensity of these signals can be almost completely accounted for by strongly dipolarly interacting spin pairs, which couple only weakly by dipolar interaction to other spins.

Two interacting P_b electrons may be described by the spin Hamiltonian

$$\mathcal{H} = g_{\parallel} \mu_B \mathbf{B} \cdot (\mathbf{S}_1 + \mathbf{S}_2) + J'' \mathbf{S}_1 \cdot \mathbf{S}_2 + \mathbf{S}_1 \cdot \vec{D} \cdot \mathbf{S}_2, \quad (22)$$

where \vec{D} is determined exclusively by the DD interaction (as $\Delta g/g$ is quite small, the anisotropic part of the superexchange is negligible). The reduction factor R for $\mathbf{B} \parallel [111]$ of the ESR P_b fine-structure signal (the expression is actually only computed for the low-field resonance, as the high-field part gives identical results) as a result of the increased population of the diamagnetic singlet state at the cost of the paramagnetic triplet spin level due to superexchange may be written as

$$R = \frac{1 + \exp(-h\nu/k_B T) + \exp[(h\nu - \frac{3}{2}D)/k_B T] + \exp[(J'' - \frac{1}{2}D)/k_B T]}{1 + \exp(-h\nu/k_B T) + \exp[(h\nu - \frac{3}{2}D)/k_B T] + \exp(-D/2k_B T)}, \quad (23)$$

where $D = (\mu_0/4\pi)(g^2 \mu_B^2 / r_{SS}^3)$, and k_B and ν represent the Boltzmann constant and microwave frequency, respectively. R is obtained from the ratio of the ESR intensities (proportional to the population difference between the two levels that make up the low-field transition) measured for the cases where $J'' \neq 0$ and $J'' = 0$, respectively. The energy-level populations and their differences are calculated in the canonical ensemble formalism using the set of energy levels obtained by solving Eq. (22). Inserting the values $J'' = 0.005-0.02$ eV, $\nu = 20.2$ GHz, and $r_{SS} = 7.68$ Å gives $R(T=4.2 \text{ K}) = 4 \times 10^{-6} - 4 \times 10^{-24}$. So the intensity of the third-neighbor fine-structure doublet, which is already weak in the absence of exchange [see the theoretical dipolar spectrum for the random-distribution model shown in Fig. 15 (S1)], is attenuated

ter will be prerequisites for any success. Neither could the resolved fine structure be detected by light excitation at 4.2 K because of the physical dimensions of the sample, consisting of a stack of about 15 platelets that prevents the light from reaching the internal Si/SiO₂ interfaces. Light excitation could probably populate the triplet levels, which are otherwise nearly empty because of the Boltzmann factor.

As a result of the superexchange-induced antiferromagnetic spin pairing, the concentration of trivalent defects ($\cdot\text{Si} \equiv \text{Si}_3$) and ESR-active P_b defects are no longer identical. This means that the measured (ESR) fractional occupancy is lower than the fractional site occupancy of nonpassivated P_b defects to be used in the calculation of the spectra. The effect is small for low f , but increases

$f = 5 \times 10^{-3}$. Figure 16 shows a high- f spectrum ($[P_b] \approx 1.2 \times 10^{13} \text{ cm}^{-2}$) spanning a 52 G range. This is the maximum intensity available by the depassivating treatments outlined. Apart from the A , B , and C lines, traces of some more structure are observed that likely result from fifth-, sixth-, and seventh-nearest-neighbor interaction. The lack of intensity and theoretical simulation, however, prevent conclusive identification. Much is expected, though, from correct simulations of these spectra as a means to obtain more-refined knowledge about the prevailing array of Si sites at the (111)Si/SiO₂ interface allowed as P_b sites, viz., the fully random-distribution model versus the partially self-avoiding P_b defect distribution. This, however, must await strongly enhanced computer calculation capacity, or, preferably, analytic solution of the line shape for a 2D system in the presence of DD interactions.

C. Comparison with other calculations using the computational approach

The computational approach for calculating dipolarly broadened resonance spectra was pioneered by Brower and Headley²⁴ in an attempt to understand line broadening within the P_b system. In particular, it was applied to separate out the DD broadening in a P_b spectrum, measured for $\mathbf{B} \parallel [111]$ on a stack of 35 (111)Si/SiO₂ platelets, each slice measuring $0.21 \times 0.23 \times 0.32 \text{ cm}^3$, and which was assigned a P_b density $[P_b] = (3-5) \times 10^{12} \text{ cm}^{-2}$, corresponding to $f \approx 0.004-0.006$. The spectrum is characterized by a width $\Delta B = 2.1 \text{ G}$ of the absorption P_b spectrum, obtained by numerical integration of the derivative spectrum of width $\Delta B_{pp} = 1.33 \text{ G}$. Their calculations, however, encountered difficulties, among others in reproducing the observed line shape and derivative width. To match the absorption linewidths, they convoluted the dipolar histogram with a Gaussian residual curve of $\Delta B = 1.75 \text{ G}$, resulting in a theoretical shape of too much Gaussian character. There appears, additionally, some inconsistency: Using a Gaussian residual profile with $\Delta B^R = 1.75 \text{ G}$ implies a residual derivative width of $\Delta B_{pp}^R = \Delta B^R / \sqrt{2 \ln 2} = 1.49 \text{ G}$. This not only exceeds our experimental values of $1.29 \pm 0.03 \text{ G}$ but also exceeds their experimental value $\Delta B_{pp}(f = 5 \times 10^{-3}) = 1.33 \text{ G}$. By comparison of the experimental and theoretical line shapes for $f = 5 \times 10^{-3}$, these workers also point out the excessive Gaussian character of the calculated resonance.

The present results may well explain their difficulties encountered in fitting the experimental spectrum. There are two shortcomings in the theoretical simulation. First, there is the fact that their calculations were carried out for the random-distribution model on a circular region of the (111)Si/SiO₂ interface containing ($N = 613$) Si-O bonding sites, i.e., possible P_b sites. It has been shown that such a region is too small to obtain accurate estimates of the dipolar broadening; Fig. 10 clearly shows that for a (111)Si surface region of $N = 613$ and for $f = 5 \times 10^{-3}$, the calculated dipolar broadening has still not reached two-thirds of the correct final value obtained for $N \rightarrow \infty$. This means that their calculated values for $N = 613$ and $f = 5 \times 10^{-3}$ are still underestimated, and

most of the underestimation will have resulted from limited computer capacity. Second, the Gaussian profile they used to represent the residual P_b line shape is inappropriate, as was demonstrated in Sec. IV B. Neither is a Lorentzian shape appropriate; the present experiments at low concentrations clearly indicate that the ratio $\Delta B / \Delta B_{pp} = 1.53 \pm 0.06 \text{ G}$ is incompatible with the values $\sqrt{2 \ln 2} = 1.18$ and $\sqrt{3} = 1.73$ for the Gaussian and Lorentzian profiles, respectively. One could argue, in support of the use of a Gaussian residual shape, that the experimental P_b resonance, measured in Refs. 23 and 24, contains a larger strain broadening than is the case for the present observations. Such a broadening is of Gaussian character. Strain broadening, however, is expected to be negligible for $\mathbf{B} \parallel [111]$.

These theoretical shortcomings, though, may not explain all of the difficulties encountered. There appears, additionally, an experimental one of even higher impact. It relates to the accuracy of the generally hard-to-realize absolute spin-density measurement, in particular for the present 2D spin system. When comparing their linewidth data to those of Fig. 2, it appears that the former would appertain to the $f \approx 0.0008-0.0009$ ($[P_b] \approx 7 \times 10^{11} \text{ cm}^{-2}$) case rather than to the quoted value $f = 0.004-0.006$. This means that an attempt has been made to fit a theoretical spectrum of too large a DD broadening. With these remarks taken into account, one finds that the theory accounts well for their superb spectrum.

A still puzzling ESR characteristic of the P_b defect regards the observation of a P_b concentration anisotropy.²³ In his work, Brower reports an intensity anisotropy factor, defined as the intensity ratio $I_{\perp}(\mathbf{B} \perp [111]) / I_{\parallel}(\mathbf{B} \parallel [111])$, of 2.0 at 35 K, 1.75 at 100 K, and 1.69 at 250 K for $\nu = 19.747 \text{ GHz}$. The presently gained understanding of the DD interaction in the P_b spectrum has prompted us to check these observations, as it was suspected that they could relate to anisotropy in the DD effects. Accurate concentration calibrations were carried out for different orientations of \mathbf{B} in the (112) plane, giving $I_{\perp} / I_{\parallel} = 1.15 \pm 0.10$ at $T = 4.2 \text{ K}$. Saturation effects were thoroughly checked. This discrepancy is not understood, although many of the measurement conditions for both experiments were similar (except for the temperature).

It needs to be remarked, though, that particular care is required when numerically integrating the experimental $dP_{\mu a} / dB$ P_b spectrum. As evidenced in this work (see, e.g., Figs. 3 and 16), increasingly more oscillator strength is shifted out of the main Zeeman resonance with increasing f , which reaches considerable proportions. Broad wings are generated, literally extending over tens of gauss. This imposes the use of a sufficiently broad field integration range so as to include all signal strengths, e.g., a 50-G range is needed for $f \approx 1\%$ to keep the error below a few percent. It is evident that one needs to be particularly on the alert for such an effect when rotating \mathbf{B} because of the varying P_b line shape resulting from admixing of anisotropic g -tensor broadening and anisotropic DD-interaction effects; this would suggest a field-direction-dependent adjustment of the integration ranges.

So, if it does not result from a measurement artifact, the intensity anisotropy remains unclear; such a large intensity anisotropy cannot be understood from the present knowledge of hyperfine, dipolar, and exchange interactions in the P_b spin system.

D. The linewidth anisotropy

The ESR linewidth anisotropy is well known to be one of the typical indications for the presence of DD and exchange interactions in one- and two-dimensional magnetic systems.^{62,66} Its nature depends on the dimensionality of the spin system, and scrutinizing experiments have been carried out on the P_b resonance in order to separate out such anisotropic effects—without any success, however.^{23,26}

The measurements and calculations, as presented in this paper, enable us to make an accurate estimate of the dipolar linewidth anisotropy of the P_b resonance. For the highest- f spectrum ($f \approx 0.015$) measured, ΔB_{pp} approximately equals 1.90 G, which corresponds to a dipolar broadening with respect to the residual profile of approximately 0.6 G for $\mathbf{B} \parallel [111]$. The dipolar broadening as a function of the magnetic-field angle $\Delta B_{pp}^D(\theta)$ can be written as

$$\Delta B_{pp}^D(\theta) = \Delta B_{pp\parallel}^D + \xi(3 \cos^2 \theta - 1)^2, \quad (24)$$

where $\Delta B_{pp\parallel}^D$ and ξ are empirical constants.⁶⁶ The ratio²⁵ of the maximum dipolar broadening, which occurs at $\theta=0$, to the minimum dipolar broadening is typically $\frac{3}{2}$ for 2D spin distributions. Hence, the maximum dipolar anisotropy of the P_b resonance linewidth ΔB_{pp} is about 0.2 G for $f \approx 0.015$. This variation is strongly overshadowed by the anisotropic linewidth variation due to strain broadening, which is at least^{23,28} ≈ 5 G. Moreover, the residual linewidth, being dominated by unresolved hyperfine broadening, may even exhibit an estimated anisotropy of at least 0.1 G. Trying to reveal the dipolar broadening in the P_b resonance by means of its linewidth anisotropy is therefore rather desperate, at least within the present state-of-the-art S/N ratio. This is particularly true for as-oxidized samples where the P_b density is only about one-third of the maximum concentration presently attainable. Variation of the spin concentration, on the other hand, has been shown to be a far more sensitive way to resolve DD interactions.

VI. SUMMARY AND CONCLUSIONS

This work has led to the separation of the effects of the DD interaction in the ESR spectrum of [111] P_b defects at the (111)Si/SiO₂ interface for $\mathbf{B} \parallel [111]$. This has been made possible by varying the P_b concentration reproducibly on a single sample by means of sequential hydrogenation and dehydrogenation treatments. To our knowledge, this also is the first observation of the dipolar line shape in a pure 2D magnetic system confined to a single atomic plane not interacting with other nearby magnetic planes. The thermal treatments in vacuum up to 835°C were

found not to influence the interface structure, thus enabling reproducible measurements of the P_b characteristics.

Measurements at extremely low concentrations ($f \approx 0.0002$ – 0.0005) revealed the residual line shape, devoid of DD interactions, which is dominated by unresolved hyperfine interactions. The knowledge of that shape is crucial, not only because it is needed as the convoluting line shape of dipolar histograms, but also because it incorporates the basis to unravel the various line-broadening mechanisms. It is characterized by $\Delta B_{pp}^R = 1.29 \pm 0.03$ G, $\Delta B^R = 1.98 \pm 0.03$ G, and $\kappa = 2.0 \pm 0.1$. Theoretical analysis of the line shape indicates that the hyperfine interaction constants, predicted by the Si₂₂H₂₇ P_b model of Cook and White,^{12,13} are somewhat underestimated. The residual experimental ESR data could not be perfectly simulated. Nor could the theoretical residual shape, when used to convolute the dipolar histograms, satisfactorily account for the higher- f experimental P_b spectra. This raises questions regarding the particular cluster model underlying these calculations. Accurate data on superhyperfine interactions will be needed to clarify this matter. These may come from ENDOR measurements or ESR observations on ²⁹Si-enriched Si substrates.

The effects of DD interactions between P_b spins are revealed with increasing f . The central Zeeman resonance gradually broadens and changes shape, while fine structure doublets develop. Fine-structure doublets resulting from the fifth-, sixth-, seventh-, and higher-order nearest-neighbor DD interaction have been identified, which bears out the discrete nature of the DD interaction within a diluted 2D spin system. The resolved structure in the line shape has been demonstrated to be the main reason why moment calculations are not suitable for predicting the dipolar linewidth.

Dipolar P_b spectra have been calculated by numerical diagonalization of the spin Hamiltonian for different arrays of Si atom sites in an unreconstructed (111)Si plane, over which the P_b 's are randomly distributed. The calculations were carried out for circular regions of a (111)Si plane containing maximally 1573 sites. Five different arrays have been studied, which were selected as a representative cross section of all plausible P_b location arrays one could suggest, based upon the present microscopical understanding of the Si/SiO₂ interface. The comparison to experimental curves gives strong evidence that the P_b defects reside at interfacial terraces and are described by a random-distribution model, that is, the array of possible sites is formed by all Si atom sites in a (111)Si plane. Small distortions from the random-distribution model, however, such as, for instance, a *small* tendency of P_b centers to cluster or to be self-avoiding, or the nonexistence of nearest neighbors, could not be excluded, mainly because of the inability to calculate higher- f dipolar spectra. Models incorporating a strong clustering of P_b defects or a decoration of the interface steps with P_b defects could be ruled out. Likewise, a perfectly tridymitelike *c*-SiO₂/Si transition was found inappropriate, though it needs to be added that only one configuration of the interfacial puckered ditrigonal rings of six SiO₄

tetrahedra has been considered. From an estimated value of the superexchange coupling constant for interacting dangling-bond-like defect electrons in bulk Si, we suggest that the absence of resolved dipolar fine structure due to first-, second-, third-, and fourth-neighbor spin-pair interaction in the P_b resonance at 4.2 K is due to spin-spin antiferromagnetic coupling. Moreover, it is predicted from the same value that this fine structure can be observed in principle at room temperature.

The shf structure of splitting $A_{\parallel}^{\text{shf}} = 14.8 \pm 0.2$ G has been unequivocally identified and discriminated from fine structure. Previous inconsistencies between experimental and theoretical data have been removed, and a consistent picture of the P_b defect distribution, line shape, and spin interaction is obtained.

The reversible passivation results point at the existence

of a constant number, i.e., $[P_b]^* \approx 1.2 \times 10^{13} \text{ cm}^{-2}$, of $\cdot\text{Si} \equiv \text{Si}_3$ defects (passivated or not) at the interface of conventional (111)Si/SiO₂ interface. This number appears as a natural constant characterizing the (111)Si/SiO₂. Yet more experiments at different oxidation temperatures will be needed to validate this finding. Together with the spin distribution, the maximum P_b concentration value and the determination of the interface stress and strain⁶⁷ may lead to a more thorough understanding of the oxidation process and the physical mechanism leading to P_b generation.

ACKNOWLEDGMENTS

The financial support by the Belgian National Fund for Scientific Research is gratefully acknowledged.

- ¹See, e.g., E. H. Poindexter and P. J. Caplan, *Prog. Surf. Sci.* **14**, 201 (1983), and references cited therein; for a recent review, see the series of papers in *Semicond. Sci. Technol.* **4**, 961 (1989).
- ²J. H. Mazur, R. Gronsky, and J. Washburn, *Proc. Soc. Photo-Opt. Instrum. Eng.* **463**, 88 (1984).
- ³J. Wollschläger and M. Henzler, *Phys. Rev. B* **39**, 6052 (1989).
- ⁴A. Ourmazd, J. A. Rentschler, and J. Bevk, *Appl. Phys. Lett.* **53**, 743 (1988).
- ⁵M. H. White and J. R. Cricchi, *IEEE Trans. Electron Devices* **ED-19**, 1280 (1972).
- ⁶Y. Nishi, *Jpn. J. Appl. Phys.* **10**, 52 (1971).
- ⁷P. J. Caplan, E. H. Poindexter, B. E. Deal, and R. R. Razouk, *J. Appl. Phys.* **50**, 5847 (1979).
- ⁸E. H. Poindexter, P. J. Caplan, B. E. Deal, and R. R. Razouk, *J. Appl. Phys.* **52**, 879 (1981).
- ⁹K. L. Brower, *Appl. Phys. Lett.* **43**, 1111 (1983).
- ¹⁰W. E. Carlos, *Appl. Phys. Lett.* **50**, 1450 (1987).
- ¹¹A. H. Edwards, *Phys. Rev. B* **36**, 9638 (1987).
- ¹²M. Cook and C. T. White, *Phys. Rev. Lett.* **59**, 1741 (1987).
- ¹³M. Cook and C. T. White, *Phys. Rev. B* **38**, 9674 (1988).
- ¹⁴E. H. Poindexter, G. J. Gerardi, M.-E. Rueckel, P. J. Caplan, N. M. Johnson, and D. K. Biegelsen, *J. Appl. Phys.* **56**, 2844 (1984); N. M. Johnson, D. K. Biegelsen, M. D. Moyer, S. T. Chang, E. H. Poindexter, and P. J. Caplan, *Appl. Phys. Lett.* **43**, 563 (1983).
- ¹⁵G. J. Gerardi, E. H. Poindexter, P. J. Caplan, and N. M. Johnson, *Appl. Phys. Lett.* **49**, 348 (1986); S. T. Chang, J. K. Wu, and S. A. Lyon, *ibid.* **48**, 662 (1986).
- ¹⁶P. M. Lenahan and P. V. Dressendorfer, *Appl. Phys. Lett.* **44**, 96 (1984); *J. Appl. Phys.* **55**, 3495 (1984).
- ¹⁷"Poor quality" is meant to refer to those Si/SiO₂ structures grown under circumstances distinctly different from the conventional ones (i.e., oxidation at $\approx 1000^\circ\text{C}$ in high-purity O₂ at ≈ 1 atm). Extreme examples are the Si/native SiO₂ structure or a Si/SiO₂ interface grown at 1000°C in an O₂ pressure of $\approx 10^{-5}$ atm.
- ¹⁸A. Stesmans, *Appl. Phys. Lett.* **48**, 177 (1986).
- ¹⁹A. Stesmans and G. Van Gorp, *Phys. Rev. B* **39**, 2864 (1989).
- ²⁰K. L. Brower, *Appl. Phys. Lett.* **53**, 508 (1988); *Phys. Rev. B* **38**, 9657 (1988); **42**, 3444 (1990).
- ²¹E. Kooi, *Philips Res. Rep.* **20**, 578 (1965); P. Balk, *Electronics Div. Electrochem. Soc.* **14**, 237 (1965); N. M. Johnson, D. K. Biegelsen, and M. D. Moyer, *J. Vac. Sci. Technol.* **19**, 390 (1981); K. L. Brower, P. M. Lenahan, and P. V. Dressendorfer, *Appl. Phys. Lett.* **41**, 251 (1982).
- ²²J. Braet and A. Stesmans, *Physica* **126B**, 563 (1984).
- ²³K. L. Brower, *Phys. Rev. B* **33**, 4471 (1986).
- ²⁴K. L. Brower and T. J. Headley, *Phys. Rev. B* **34**, 3610 (1986).
- ²⁵J. Braet, Ph.D. thesis, Katholieke Universiteit Leuven, 1985.
- ²⁶K. L. Brower, in *Proceedings of the 13th International Conference on Defects in Semiconductors*, edited by L. C. Kimmerling and J. M. Parsey, Jr. (The Metallurgical Society of AIME, Warrendale, PA, 1985), p. 485.
- ²⁷A. Stesmans and J. Braet, *Surf. Sci.* **172**, 389 (1986).
- ²⁸A. Stesmans and J. Braet, in *Insulating Films on Semiconductors*, edited by J. J. Simonne and J. Buxo (North-Holland, Amsterdam, 1986), p. 25.
- ²⁹A. Stesmans, *J. Magn. Res.* **76**, 14 (1988).
- ³⁰A. Stesmans and Y. Wu, *J. Phys. D* **21**, 1205 (1988).
- ³¹A. Stesmans and G. Van Gorp, *Phys. Lett. A* **139**, 95 (1989); *Rev. Sci. Instrum.* **60**, 2949 (1989).
- ³²This conclusion merely relies on the fact that—along the evidence—H is the main passivating agent of interface defects. Some defects, of course, could be passivated differently, e.g., by Cl, F, etc. If these would appear less affected by the applied depassivating treatments, then $[P_b]_{\text{max}}$ rather represents an underbound for $[P_b]^*$. However, the much-lower probability for such impurities in the Si/SiO₂ system is felt to make their contribution negligible.
- ³³A. Stesmans and G. Van Gorp, *Appl. Phys. Lett.* **57**, 2663 (1990).
- ³⁴See, e.g., W. A. Pliskin and R. A. Gdula, in *Handbook on Semiconductors*, edited by S. P. Keller (North-Holland, Amsterdam, 1980), Vol. 3, p. 641.
- ³⁵This is in contrast with previous work (see Ref. 20) stating that the P_b density in as-oxidized (111)Si/SiO₂ structures is unaffected by subsequent thermal anneals in vacuum at temperatures extending up to 850°C .
- ³⁶A. Stesmans, *Z. Phys. Chem. Neue Folge* **151**, 191 (1987).
- ³⁷T. G. Castner, *Phys. Rev.* **115**, 1506 (1959).
- ³⁸J. H. Van Vleck, *Phys. Rev.* **74**, 1168 (1948).
- ³⁹C. Kittel and E. Abrahams, *Phys. Rev.* **90**, 238 (1953).
- ⁴⁰G. W. Canters and C. S. Johnson, *J. Magn. Res.* **6**, 1 (1972).

- ⁴¹G. W. Parker, *Am. J. Phys.* **38**, 1432 (1970).
- ⁴²P. W. Anderson, *Phys. Rev.* **82**, 342 (1951).
- ⁴³N. Bloembergen, E. M. Purcell, and R. V. Pound, *Phys. Rev.* **73**, 679 (1948).
- ⁴⁴A. Carrington and A. McLachlan, *Introduction to Magnetic Resonance* (Harper and Row, New York, 1967), p. 32.
- ⁴⁵A. Stesmans, *Appl. Surf. Sci.* **30**, 134 (1987).
- ⁴⁶W. E. Carlos, in *The Physics and Technology of Amorphous SiO₂*, edited by R. A. B. Devine (Plenum, New York, 1988), p. 259.
- ⁴⁷G. D. Watkins and J. W. Corbett, *Phys. Rev.* **134**, 1359 (1964).
- ⁴⁸Y.-H. Lee and J. W. Corbett, *Phys. Rev. B* **8**, 2810 (1973).
- ⁴⁹P. L. Scott and C. D. Jeffries, *Phys. Rev.* **127**, 32 (1962); P. R. Cullis, *J. Magn. Res.* **21**, 397 (1976).
- ⁵⁰K. L. Brower, *Z. Phys. Chem. Neue Folge* **151**, 177 (1987).
- ⁵¹G. Feher, *Phys. Rev.* **114**, 1219 (1959).
- ⁵²W. Kohn and J. M. Luttinger, *Phys. Rev.* **97**, 1721 (1955); **98**, 915 (1955).
- ⁵³Abragam and Bleaney, *Electron Paramagnetic Resonance of Transition Ions* (Clarendon, Oxford, 1970).
- ⁵⁴P. W. Anderson, in *Solid State Physics*, edited by F. Seitz and D. Turnbull (Academic, New York, 1963), Vol. 14, p. 99.
- ⁵⁵T. Moriya, *Phys. Rev.* **120**, 91 (1960).
- ⁵⁶Y.-H. Lee and J. W. Corbett, *Phys. Rev.* **13**, 2653 (1976).
- ⁵⁷C. P. Slichter, *Principles of Magnetic Resonance* (Harper and Row, New York, 1963), p. 46.
- ⁵⁸This elaborate quantum-mechanical computational approach is chosen rather than the simple magnetostatic local-field model calculation (see Ref. 41) to take into account spin-correlation effects.
- ⁵⁹J. M. Gordon, M. Y. Lanzerotti, and V. Elser, *Appl. Phys. Lett.* **55**, 1394 (1989).
- ⁶⁰F. J. Grunthaner, P. J. Grunthaner, R. P. Vasquez, B. F. Lewis, and M. Maserjian, *J. Vac. Sci. Technol.* **16**, 1443 (1979).
- ⁶¹J. H. Konnert, J. Karle, and G. A. Ferguson, *Science* **179**, 177 (1973); J. H. Konnert, P. d'Antonio, and J. Karle, *J. Non-Cryst. Solids* **53**, 135 (1982).
- ⁶²M. J. Hennessey, C. D. McElwee, and P. M. Richards, *Phys. Rev. B* **7**, 930 (1973).
- ⁶³The origin of structural differences between spectra 1 and 3 (random-distribution model and ditrigonal-ring model, respectively), though calculated on the "same" lattice but with different lattice constants, is clear when looking at Fig. 10. In terms of the random-distribution array of possible P_b sites [i.e., all Si sites in a (111)Si plane], the fifth- to the twelfth- (and also first-, second-, and third-) nearest-neighbor positions are not allowed in the ditrigonal-ring model array. The histograms calculated for both cases will of course have identical shapes, but with significantly differing field scales. This results in different line shapes when convoluting both histograms with the same broadening function of $\Delta B_{pp}^R = 1.29$ G. Moreover, the effective f in both models differs by a factor of 7.
- ⁶⁴K. L. Brower, *Phys. Rev. B* **4**, 1968 (1971); **5**, 4274 (1972).
- ⁶⁵W. Jung and G. S. Newell, *Phys. Rev.* **132**, 648 (1963).
- ⁶⁶P. M. Richards and M. B. Salamon, *Phys. Rev. B* **9**, 32 (1974).
- ⁶⁷C. H. Bjorkman, J. T. Fitch, and G. Lucovsky, *Appl. Phys. Lett.* **56**, 1983 (1990).